Key Points:
- Fault slip behavior is mainly controlled by roughness and asperity nucleation size
- Plastic deformation can coexist with the occurrence of laboratory earthquakes
- Fault weakening initiation depends on asperity hardness while weakening efficiency depends on melt viscosity

Correspondence to:
J. Aubry,
jerome.aubry@ens.fr

Fault Stability Across the Seismogenic Zone

J. Aubry[1] , F. X. Passelègue[2], J. Escartín[1], J. Gasc[1], D. Deldicque[1], and A. Schubnel[1]

[1]Laboratoire de Géologie, École Normale Supérieure/CNRS UMR 8538, PSL Research University, Paris, France, [2]École Polytechnique Fédérale de Lausanne, Lausanne, Switzerland

Abstract Across the seismogenic zone, the transition from brittle to plastic deformation corresponds to a semibrittle regime where brittle fracturing and plastic flow coexist at high strength conditions. Thorough experimental investigations on brittle-plastic transition are crucial to understand why natural faults behave in stable or unstable ways at varying crustal depths and why large earthquakes generally nucleate at the base of the seismogenic zone. To investigate semibrittle deformation in carbonates and the conditions promoting it, we reported here the results of experiments performed on Carrara marble saw cut faults in triaxial conditions. We studied the influence of the confining pressure (ranging between 45 and 180 MPa), axial loading rates (0.01 and 1 μm s^{-1}) and initial fault roughness (smooth and rough) on fault (in-)stability across the brittle-plastic transition. We conclude that laboratory earthquakes may nucleate on inherited fault interfaces at brittle-plastic transition conditions. The occurrence of laboratory earthquakes associated with increasing plastic deformation is promoted at high confining pressure, on smooth fault interfaces, or when the loading rate is slow. In a rather counterintuitive manner, increasing initial roughness promotes stable sliding and a larger amount of plastic deformation. Furthermore, we show that stable sliding tends to produce mirror-like surfaces, while stick-slips are associated with matte surfaces, on which the size of the asperities grows with increasing confining pressure. Finally, our results seem to reveal the influence of asperity hardness and melt viscosity on fault weakening.

Plain Language Summary The regime where both brittle and plastic deformation processes are active is known as the semibrittle regime. Understanding fault stability within this regime is crucial because large earthquakes nucleate at the base of this intermediate regime. To look at the slip behavior of fault surfaces within the semibrittle regime, we performed experiments on simulated faults made of Carrara marble, a rock standard prone to be deformed in the semibrittle field at room temperature and pressure conditions of the Earth's upper crust in the laboratory. Through distinctive seismic cycle experiments on artificial laboratory faults, we investigated slip behavior (stable slip, slow slip, or stick-slip) as a function of pressure, background loading rates, and initial roughness. We conclude that (i) fault slip behavior is controlled by fault roughness, (ii) plastic deformation can coexist with the occurrence of laboratory earthquakes (i.e., unstable faults) within the semibrittle regime, and (iii) asperity hardness and melt viscosity influence slip weakening.

1. Introduction

The recent discovery of a broad range of fault slip behaviors from slow to fast velocities (Obara & Kato, 2016; Passelègue et al., 2019; Peng & Gomberg, 2010) has shed a new light on the heterogeneous character of natural faults. Although observed, this spectrum of fault slips is not completely understood in terms of physical mechanisms. From the weakening stage to the observation of a repetitive slip pattern during the seismic cycle, the dynamics of sliding controls the stability of faults across the seismogenic zone.

From shallow to deep, two distinct deformation regimes, called brittle and plastic, influence fault stability and reactivation. From friction laws, the limit between the brittle and plastic deformation fields has been interpreted as a limit between velocity weakening (stable regime) and velocity strengthening (unstable regime) friction (Shimamoto & Logan, 1986; Tse & Rice, 1986). Faults are theoretically known to be unstable in the upper crust because rock deformation is accommodated by brittle mechanisms, such as frictional sliding and microfracturing, inducing strain localization along crustal faults. Conversely, in the lower crust (typically at depth greater than 20 km), faults are expected to be more stable since deformation is accommodated by (temperature dependent) intracrystalline plasticity (e.g., by twinning, grain boundary diffusion, or dislocation glide), which may be distributed within the rock (Paterson & Wong, 2005).

Between these two distinct end-members, brittle and plastic deformation mechanisms coexist in a transitional semibrittle regime (Evans et al., 1990; Fredrich et al., 1989). From plastic flow laws, the top of the semibrittle layer has been defined as the depth at which the pressure and temperature conditions allow plastic processes to initiate at natural plate boundary strain rates (De Bresser & Spiers, 1997; Hirth & Tullis, 1994; Kohlstedt et al., 1995). This regime is critical because large earthquakes nucleate and propagate within the semibrittle regime (Das & Scholz, 1983; Hobbs & Ord, 1988; McNulty, 1995). However, the interactions between brittle and plastic deformation processes regarding fault weakening and stability within this deformation regime remain unclear.

Because calcite is prone to deform plastically at room temperature under relatively moderate confining pressures (De Bresser & Spiers, 1997; Fredrich et al., 1989), carbonates can be used to investigate earthquake nucleation within the semibrittle regime. An extensive number of laboratory studies have experimented the transition from brittle to semibrittle rock deformation in intact carbonates (Fredrich et al., 1989; Nicolas et al., 2017; Schubnel et al., 2006; Vajdova et al., 2004, 2010; Wong & Baud, 2012), carbonate fault gouges (Smith et al., 2015; Verberne et al., 2013, 2014, 2015), or carbonate saw cut samples (Harbord, 2018; Passelègue et al., 2019). Studies on intact samples highlighted a transition from localized to ductile (i.e., distributed) deformation with increasing confining pressure. At low sliding velocities, fault gouge and saw cut experiments highlighted the velocity strengthening behavior of calcite, the formation of slicken-sides or mirror-like surfaces (Fondriest et al., 2013), similar to that observed in the field (Siman-Tov et al., 2013) and a transition to velocity weakening with increasing temperature (Passelègue et al., 2019; Verberne et al., 2015).

While this transition from brittle to plastic deformation mechanisms is primarily controlled by pressure and temperature (Fredrich et al., 1989), fault roughness may also play a key role as it controls the actual stress conditions at contacting asperities, the geometry of localized asperities, and thus fault weakening. The influence of fault roughness on slip behavior has been studied from natural observations (Bistacchi et al., 2011; Jolivet et al., 2013; Sagy et al., 2007), numerical models (Fang & Dunham, 2013; Zielke et al., 2017), and rock mechanics experiments (Harbord et al., 2017; Renard et al., 2012).
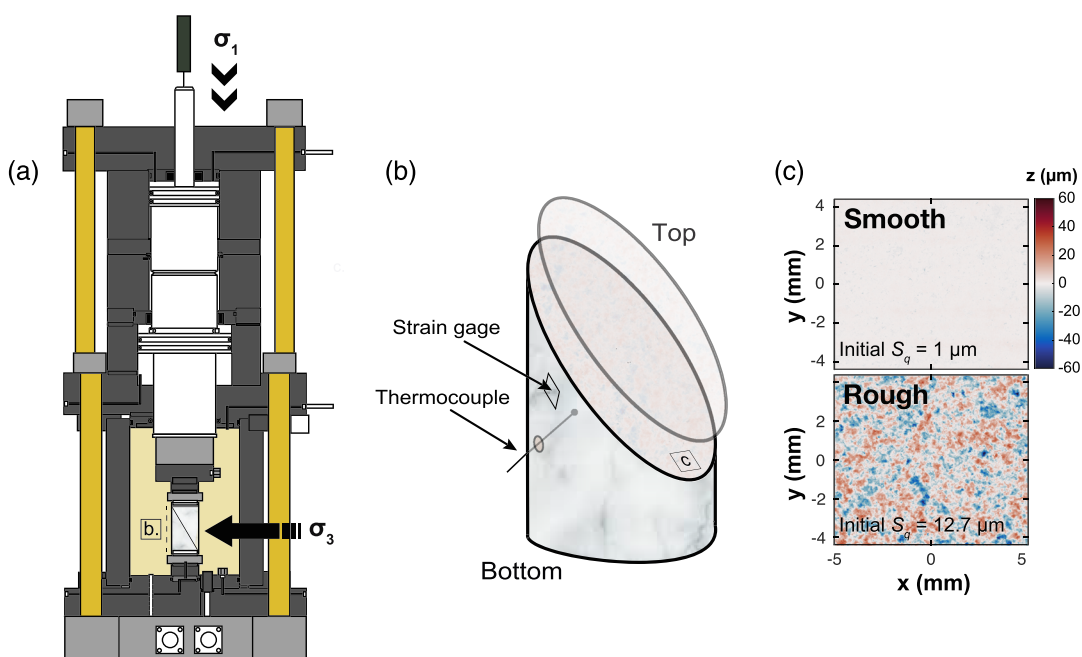
In this study, we investigate the macroscopic and microscopic behaviors of Carrara marble laboratory faults to understand earthquake nucleation, fault stability, and the interactions between brittle and plastic processes within the semibrittle regime. Carrara marble is easily found in the central Apennines (Meccheri et al., 2007), a region where destructive earthquake swarms (Chiarabba et al., 2009; Galli et al., 2008) coexist with slow aseismic sliding (Amoruso et al., 2002; Scarpa et al., 2008).

We performed 14 triaxial deformation experiments on saw cut cylindrical specimens deformed under varying confining pressure (45, 90, and 180 MPa), loading rates (0.01 and 1 μm s^{-1}), and initial fault roughness conditions (smooth or rough). In addition, we imaged the evolution of fault surfaces using surface profilometry and microanalysis equipment. In light of our results, we finally discuss earthquake nucleation, fault stability, and strain partitioning across the brittle-plastic transition.
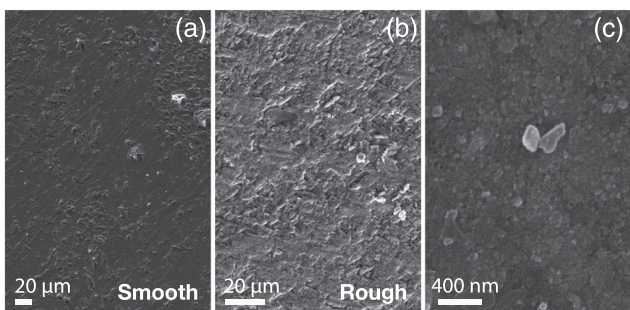
2. Materials and Methods

2.1. Sample Characterization and Preparation

The starting material used in the experiments is a type C-D Bianco Carrara Marble, from Apuan Alps (Carrara, Italy). This rock, a standard in rock mechanics is composed of calcite grains (>98%, 150 μm average grain size) and accessory grains of quartz, pyrite, and epidote of few microns in diameter (Fredrich et al., 1989). We used cylindrical samples (80 mm in length and 40 mm in diameter) with a saw cut interface at 30° with respect to the vertical axis (Figure 1b). After cutting, each side of the interface is flattened with a surface grinder and roughened either with #1200 or #50 wet silicon carbide grit sandpapers. This resulted in initial average RMS roughness S_q of 1 and 12.7 μm for the initially smooth and rough fault interfaces, respectively (Figure 1c; see section 4.2). Roughening stage was performed for only 3 min in order to minimize the formation of nanograins and amorphous material. Nevertheless, SEM imaging of fault interfaces at the end of the polishing process revealed irregular surfaces with nanoparticles of calcite, supposed to be produced by mechanical abrasion (Figure 2).

Figure 1. Sample preparation and experimental device. (a) Schematics of the triaxial apparatus used at ENS. Modified from Fortin et al. (2007), Schubnel et al. (2005), and Aubry et al. (2018). σ_1 and σ_3 are the axial and radial stresses acting on the sample, schematized in (b). The direction of sliding is toward bottom. (b) Schematic of the saw cut sample. Strain gages are glued on the sample and a thermocouple is inserted in the sample 1 to 2 mm away from the fault surface (only for smooth samples). The initial roughness of the fault is decided before the experiment. (c) Initial roughness applied on the two parts of the fault before experiments. The initial roughness map shown on top corresponds to the smooth interfaces studied here (initial RMS roughness $S_q = 1$ μm, labeled smooth). The bottom roughness map corresponds to the rough interfaces studied here (initial RMS roughness $S_q = 12.7$ μm, labeled rough). The color bar represents the altitude z of asperities (in μm).

In addition, a thermocouple was inserted 1–2 mm away from the fault surface in order to record temperature evolution (Figure 1b), in a similar way as that of previous studies (Aubry et al., 2018; Lockner et al., 2017). Only smooth fault interfaces were equipped with thermocouple. Strain gages (8.2×8 mm, 120 Ω, FCB-2-11-F type, Tokyo Sokki Kenkyujo Co., Ltd, Japan) were glued directly onto the rock surface (close to the thermocouple location) to record axial and radial strains during the triaxial experiments (maximum record of 4% deformation; Figure 1b). The sample was isolated from the oil confining medium using a neoprene jacket of 5 mm wall thickness.

Figure 2. SEM micrographs before experiments. (a) SEM micrograph of the initially smooth fault surface after grinding, polished with silicon carbide and roughened with #1200 grit sandpaper during 3 min in presence of water. (b) SEM micrograph of the initially rough fault surface after grinding, polished with silicon carbide and roughened with #50 grit sandpaper during 3 min in presence of water. (c) SEM micrographs of the fault surface at the nanoscale after the grinding stage. The presence of nanograins is observed on the initial lithology, before experiments.

2.2. Experimental Setup and Parameters Recorded During the Experiments

The triaxial cell used for these experiments is an autocompensated oil-loaded triaxial cell with an approximated stiffness of 1 MN mm^{-1}, installed at the Laboratoire de Géologie de l'École Normale Supérieure, Paris, France (Figure 1a; Aubry et al., 2018; Fortin et al., 2007; Schubnel et al., 2005). During compression, the total axial shortening D_{LVDT} was measured by an external linear variable differential transducer (i.e., LVDT, mm) and was approximately of 5 mm at the end of all experiments. Experiments were conducted at constant axial displacement rate while maintaining the confining pressure constant (resolution of ± 0.5 MPa). Two different loading rates, from slow to fast (0.01 and 1 μm s^{-1}), were investigated. These loading rates refer to the axial displacement rate of the piston as measured by the LVDT before stiffness correction. True sample axial shortening was computed by correcting the external axial measurement for machine stiffness. All displacements discussed in the following

Table 1
Summary of Experiments and Mechanical Parameters

N° expt	Main slip regime	Stress drop[a] (MPa)	Peak normal stress, σ_{np} (MPa)	Peak fault friction, μ	Displacement[a], D (mm)	Total slip (mm)	RMS roughness[b], S_q (µm)	Bulging
SF45$_{f1}$	Stable (SS + SSE)	–	57.6	0.38	–	5	2.26	No
SF45$_{f2}$	Stable (SS + STE)	–	58.36	0.36	–	5	1.14	No
SF90$_{f1}$	Stable (SS + SSE)	–	106	0.23	–	5	1.44	No
SF90$_{f2}$	Stable (SS + STE)	–	111	0.33	–	5	4.21	No
SF180$_f$	Unstable (STE)	17.4/22.2	264	0.45	0.31/0.37	1.77	4.58	Yes
SF45$_s$	Unstable (SSE)	0.7/1.6	60.2	0.38	0.02/0.03	5.8	7.02	No
SF90$_s$	Unstable (SSE + STE)	0.1/13.3	135.3	0.57	0.01/0.28	5.0	2.33	Yes
SF180$_s$	Unstable (STE)	1.42/25	247.4	0.45	0.02/0.32	1.62	4.88	Yes
RF45$_f$	Stable	–	85.5	0.79	–	4.43	37.51	Yes
RF90$_f$	Stable	–	149.8	0.66	–	3.18	19.62	Yes
RF180$_f$	Stable	–	259.3	0.51	–	0.80	11.85	Yes
RF45$_s$	Stable	–	81.5	0.73	–	5	6.19	Yes
RF90$_s$	Unstable (SSE)	0.3/1.9	140	0.55	0.02/0.05	5.6	9.09	Yes
RF180$_s$	Stable	–	252.1	0.37	–	3.07	13.77	Yes

Note. For each experiment, we detail the confining pressure (45, 90, or 180 MPa), the initial roughness (SF for smooth fault and RF for rough fault), the loading rates (f for fast and s for slow), and the main slip regime: stable or unstable. In some cases, fault reactivation and different slip regimes are observed during the same experiment. For each main slip regime, we also detail the type of events observed during the experiments (STE: stick–slip event, SSE: slow–slip event, and SS: stable sliding).
[a]For instable slip regime, D (i.e., the displacement at the end of static stress drop) is described as a range of minimum/maximum single displacement when multiple events were performed during the experiment; as for stress drops values.   [b]The initial roughness RMS roughness S_q of initially smooth and rough faults are 1 and 12.7, respectively, and compared to RMS roughness at the end of experiments. Axial shortening has been imposed close to 5 mm during the experiments. The cumulative slip on fault is the slip corrected for rock and machine elasticity. If the cumulative slip on the fault is lower that the axial shortening imposed (5 mm), the fault has been locked during the experiment and bulging may be observed.

correspond to the displacement D recorded for each static stress drop (i.e., overall reduction in shear stress on fault due to slip) and projected along the fault plane. In order to discuss strain partitioning, total axial strain δ_{LVDT} (%) was measured using the LVDT and compared to the local axial strain δ_{SG} (%) measured using strain gages. In the following, strain partitioning is defined as the ratio of local matrix strain δ_{SG} to total sample axial strain δ_{LVDT}.

Axial (σ_1) and confining (σ_3) stresses (resolution of ±0.5 MPa), displacements (±0.1 µm), strains ($\pm10^{-5}$), and temperature ($\pm0.05°C$) were all recorded at a sampling rate of 10 Hz during the experiments. Hereafter, the normal (σ_n) and shear (τ) stresses (MPa) acting on the fault interface result from the projection of the principal stress on the fault plane. Fault friction μ is thus defined as the ratio between shear and normal stresses resolved on the fault plane. Mechanical data are summarized in Table 1 for all the experiments performed in this study. Strain partitioning and shortening data are summarized in Table 2. Thermocouple data are summarized in Table 3.

2.3. Postmortem Analysis

After the experiments, several microanalysis observations were performed. First, the microtopography of each sample (top and bottom fault surfaces) was measured before and after the experiments using a noncontact surface profilometer at the Centre de Recherche et de Restauration des Musées de France in Le Louvre (Paris, France). Microtopography data were acquired over an area of 20×9 mm from a same starting point. Scanning velocity was 1,597 µm s^{-1} and measuring steps along x and y axes were 4.88 µm. Raw microtopography data were then processed with the MountainsMap (DigitalSurf, Besançon, France) and Matlab softwares. When a topographic spot was not measurable at a given location on the fault surface during

Table 2
Strain Partitioning of Laboratory Earthquakes

N° experiment	δ_{LVDT} (%)	δ_{SG} (%)	Strain partitioning, $\delta_{SG}/\delta_{LVDT}$ (%)
SF45$_{f2}$	5.53	0.04	0.007
SF90$_{f2}$	5.65	0.07	0.012
SF180$_f$	5.69	3.74	0.65
SF45$_s$	5.68	0.01	0.001
SF90$_s$	5.63	0.49	0.08
SF180$_s$	5.22	3.57	0.68
RF45$_f$	5.78	1.28	0.22
RF90$_f$	5.78	2.86	0.49
RF180$_f$	4.62	3.63	0.78
RF45$_s$	5.71	0.73	0.12
RF90$_s$	5.8	2.19	0.37
RF180$_s$	5.67	2.41	0.42

Note. Total axial strain δ_{LVDT} (%) was measured using the LVDT (measure of fault and bulk deformation) and compared to the local axial strain δ_{SG} (%) measured using strain gages (only measuring bulk deformation).

Table 3
Summary of the Thermocouple Data Analysis

N° experiment	Stress drop (MPa)	D (mm)	Thermocouple increase, T_i (°C)	E_{tot} (J m^{-2})	Q_{th} (J m^{-2})	R (%)	Temperature estimate, T_{th}(°C)
SF90$_{f2}$	18.3	0.31	0.37	8,240	7,068	0.86	294
SF90$_s$	6.3	0.14	0.21	3,989	3,312	0.83	113
SF90$_s$	6.0	0.14	0.21	4,063	3,445	0.85	118
SF90$_s$	5.2	0.12	0.18	4,630	4,240	0.92	145
SF90$_s$	7.0	0.14	0.26	8,920	6,625	0.74	225
SF90$_s$	13.8	0.28	0.33	19,558	11,130	0.57	379
SF180$_f$	17.4	0.30	0.70	29,153	7,933	0.27	330
SF180$_f$	22.3	0.38	0.86	37,835	10,097	0.27	421
SF180$_s$	28.4	0.51	0.29	46,286	11,539	0.25	480
SF180$_s$	29.8	0.36	0.40	34,783	12,261	0.35	510
SF180$_s$	28.5	0.34	0.32	33,252	12,982	0.39	540

scanning (e.g., holes or poorly reflective areas), the topography was interpolated from neighboring areas. In the following, we only present the interpolated microtopography data of footwall interfaces, expected to be representative of both sides of the fault.

Scanning electron microscopy (SEM Σigma, Ecole Normale Supérieure, Laboratoire de Géologie, Paris, France) was used to image the fault surface at the microscale and the nanoscale after each experiment. Samples were systematically gold coated. Electron backscattering diffraction (EBSD; Oxford instruments, Ecole Normale Supérieure, Laboratoire de Géologie, Paris, France) mapping was performed on some specimens, on cross sections going from the fault interface to 3–4 mm within the footwall. Measurement steps were 1 µm both in the directions parallel and perpendicular to slip. EBSD data were analyzed using the MTEX toolbox (Bachmann et al., 2010) on Matlab. Grain misorientations were inferred using the crystal parameters of calcite. Finally, transmission electron microscopy (TEM, JEM 2011 UHR/EDX, Institut des Matériaux, Paris, France) was performed on focused ion beam sections collected along the fault interface to image rock deformation at the nanoscale.
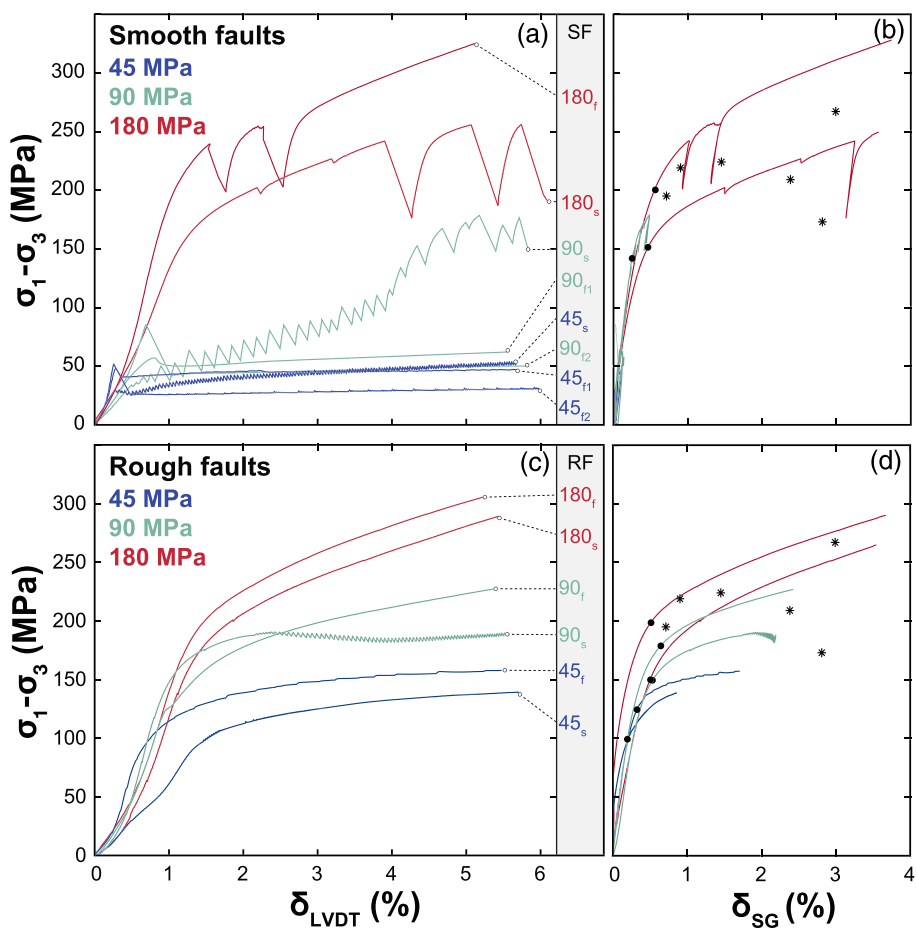
3. Results

We report here the results of 14 experiments performed at confining pressures of 45, 90, and 180 MPa, loading rate velocities of 0.01 and 1 µm s^{-1}, either on initially smooth or rough fault interfaces. Each mechanical curve is associated with the experiment run name: SF for "smooth fault," RF for "rough fault," a number indicating the confining pressure tested (45 MPa in blue, 90 MPa in green, and 180 MPa in red) and a first letter subscript showing if the experiment has been performed under fast (1 µm s^{-1}, f subscript) or slow (0.01 µm s^{-1}, s subscript) velocities. See Table 1 for more details on these experiments.

3.1. Mechanical and Temperature Data

Stress–strain curve relationships are presented in Figure 3. Fault and bulk deformations (δ_{LVDT}) refer to the total axial shortening of the samples. Bulk deformation (δ_{SG}) corresponds to the strain measured locally by strain gages. Note that the difference between the two is that the external measurement of the axial displacement recorded the total shortening of the sample, including fault slip, while local strains only measured elastic and plastic contributions to shortening (both terms were also included in total strain measurements).

3.2. Mechanical Data on Smooth Faults

During experiments conducted at low pressures of 45 and 90 MPa and a loading rate of 1 µm s^{-1} (SF45$_{f1}$, SF45$_{f2}$, SF90$_{f1}$, and SF90$_{f2}$), a first initial elastic loading was observed, up to a critical point at which a single stress drop event occurred. This event was followed by a stable slip regime until the end of the experiments on smooth fault interfaces (Figure 3a). For these experiments, peak fault friction coefficients μ ranged between 0.23 and 0.38, stress drops ranged between 2.9 and 19 MPa and displacements D ranged between 0.04 and 0.28 mm (Table 1). Stress drop was either very fast with a stick-slip (audible) or over few seconds with slow slip (inaudible). At 180 MPa confining pressure (SF180$_f$), the behavior of the fault interface differed (Figure 3a). Stress–strain relationship first increased linearly and departed from it beyond a critical

Figure 3. Mechanical data for the experiments performed on smooth and rough faults. Mechanical data for smooth faults (SF; a and b) and for rough faults (RF; c and d). Each mechanical curve is associated to the experiment run name (see coding in section 3). (a–c) Differential stress ($\sigma_1 - \sigma_3$) as a function of the total axial strain δ_{LVDT} (fault and bulk deformation) for the experiments performed on smooth a and rough c faults. The displacement plotted here is corrected for machine elasticity only. Strain data are in good agreement with data from Fredrich et al. (1989) in the background: The stars represent maximum ($\sigma_1 - \sigma_3$) and total strain reached during their experiments with intact samples of Carrara marble for confining pressure between 50 and 120 MPa. (b–d) Differential stress ($\sigma_1 - \sigma_3$) as a function of local strain δ_{SG}, the bulk deformation measured by strain gages for the experiments performed on smooth (b) and rough d faults. At low confining pressure, the fault regime deformation is quasi entirely elastic. In the other hand, at high confining pressure, most of the strain accumulated in the sample during the first stage of slip is accommodated in the bulk sample: The faults deform "plastically" when the yield stress is reached (marked with a black dot on strain gages records). Plasticity is promoted at high confining pressure and slow loading rates. For the smooth fault deformed at high pressure, we show that laboratory earthquakes can nucleate when the fault remains locked. For rough faults, we show that stable sliding and plasticity are generally promoted with increasing confining pressure and fault roughness. However, rough faults may reactivate, in particularly at intermediate pressure and slow loading rates. Gages could not record more than 4% of deformation and in some cases, stopped before the end of the experiments (i.e., before the maximum stress seen by the LVDT), explaining stress differences between subplots.

yield stress (marked with a black dot in Figure 3b) after which stick-slips prevailed at a maximum differential stress of about 250 MPa (Figure 3a). Compared to results obtained at lower confinement, higher peak fault friction coefficients (between 0.35 and 0.45), static stress drops (between 17.4 and 22.2 MPa), and single event fault displacements (between 0.32 and 0.37 mm) were observed (Table 1).

At a loading rate of 0.01 μm s^{-1}, stick or slow slips sequences were systematically observed (Figure 3a). At 45 MPa (SF45$_s$), 142 slow slips occurred at peak differential stresses ranging between 25 and 50 MPa (Figure 3a), corresponding to peak fault friction ranging between 0.22 and 0.38. Displacements for each single slow slip ranged from 0.02 to 0.04 mm, with static stress drops between 0.7 and 1.6 MPa (Table 1). At

90 MPa confining pressure (SF90$_s$), 29 stick-slip events were recorded, showing a substantial hardening above yield stress around 140 MPa (Figure 3a). For this experiment, individual stress drops ranged from 0.1 to 13.3 MPa, peak fault friction coefficients ranged from 0.15 to 0.57, and single displacements ranged from 0.01 to 0.28 mm (Table 1). At 180 MPa (SF180$_s$), five stick-slips were observed at a differential stress of 200 to 250 MPa (Figure 3a), with static stress drops of 1.4–25 MPa, coseismic displacements of 0.02–0.32 mm and an average fault friction of ~0.4 (Table 1).

Independently of the loading rate (i.e., both at 0.01 or 1 μm s^{-1}), local plastic strain recorded by strain gages δ_{SG} was negligible at 45 MPa (Figure 3b). At 90 MPa, strain gages measured up to 0.5% permanent (plastic) strain for the experiment performed at slow loading rate (SF90$_s$), highlighting a strain partitioning between fault slip and plastic strain (Figure 3b and Table 2). At 180 MPa (SF180$_f$ and SF180$_s$), strain gages measured up to 3.5% strain independently of the loading rates (Figure 3b and Table 2). This last observation demonstrates that at relatively high pressure conditions, most of the sample shortening was accommodated by plastic deformation within the bulk of the specimen rather than by fault slip.

3.3. Mechanical Data on Rough Faults

Increasing fault roughness promotes stable sliding, strain hardening, and plastic deformation when compared to the experiments conducted on smooth fault surfaces (Figure 3c). At a loading rate of 1 μm s^{-1}, stable sliding was observed between 45 and 180 MPa confining pressure (RF45$_f$, RF90$_f$, RF180$_f$). The peak differential stresses were systematically above yield stress and reached, after hardening, higher values than those reached on smooth faults (Figure 3a). Fault friction coefficients μ ranged between 0.79 at 45 MPa and 0.51 at 180 MPa (Table 1). Strain partitioning between fault slip and plastic strain in the bulk was also systematically observed, with an increasing plastic strain δ_{SG} of 1.2%, 2.8%, and 3.6% at 45 (RF45$_f$), 90 (RF90$_f$), and 180 MPa (RF180$_f$), respectively (Figure 3d and Table 2).

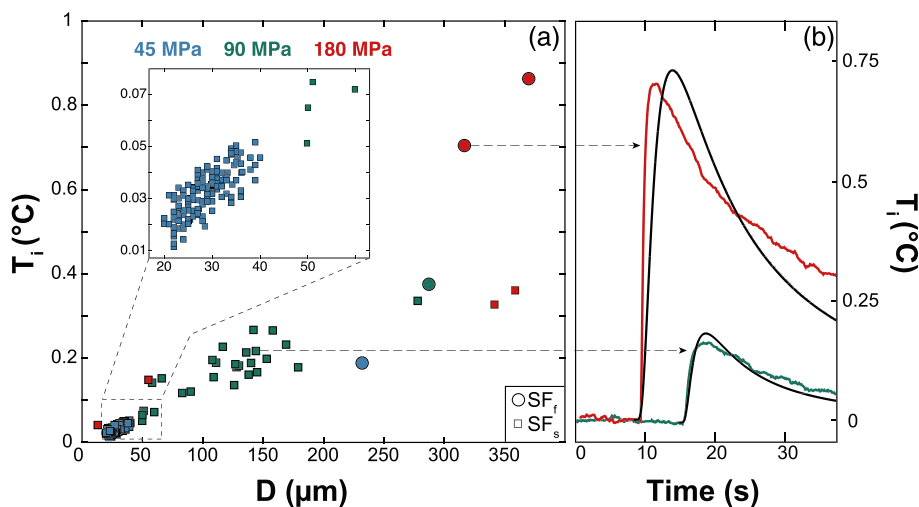A slow loading rate (0.01 μm s^{-1}) favored the reactivation of the fault in the form of small detectable instabilities during the overall stable sliding regime, principally at 90 MPa (RF90$_s$; Figure 3c). For this specific experiment, static stress drops ranged between 0.3 and 1.89 MPa and are lower than for smooth faults at the same confining pressures (Table 1). Individual fault event displacements D ranged between 0.02 and 0.05 mm at 90 MPa (Table 1). At this slow loading rate, permanent stable sliding was observed at 45 and 180 MPa (RF45$_s$ and RF180$_s$; Figure 3c), without any strong fault reactivation. Fault friction evolved from ~0.7 at 45 MPa (RF45$_s$), to ~0.55 at 90 MPa (RF90$_s$) and finally ~0.37 at 180 MPa (RF180$_s$; Table 1). Strain partitioning between fault slip and plastic strain within the bulk was also observed at this slow loading rate, with plastic strain δ_{SG} from 0.7% to 2.4% between 45 and 180 MPa (Figure 3d and Table 2).

3.4. Footwall Temperature Evolution

Temperature evolution was measured within the footwall of fault interfaces, 1–2 mm away from the fault plane with a thermocouple, only during experiments on SF. Stick-slip temperature peaks are correlated with coseismic slip, loading rates and confining pressure (Figure 4a). Temperature increases T_i ranged from 0.18°C to 0.86°C for the experiments conducted at a loading rate of 1 μm s^{-1} and from 0.01°C to 0.4°C for the experiments performed at a loading rate of 0.01 μm s^{-1} (Figure 4a). Some of these representative temperature measurements allowed us to estimate the amount of frictional heating produced during individual stick-slip (Figure 4b and Table 3). Two examples illustrating the evolution of temperature during stick-slip events performed at 90 (SF90$_s$) and 180 MPa (SF180$_f$) are displayed on Figure 4b. At 90 MPa, a temperature increase of 0.21°C was recorded during a shear stress drop of 6 MPa (Table 3). At 180 MPa, a temperature increase of 0.7°C was measured for a shear stress drop of 17.4 MPa (Table 3). In both cases, the temperature progressively decreased after stick-slip, because of heat diffusion within the bulk of the sample.

4. Microstructural Analysis

To investigate the deformation mechanisms active during the experiments, several microanalysis techniques were used: (i) microtopography using surface profilometry before and after each experiment (Figure 6), (ii) SEM and TEM imaging (Figures 7–9) of the fault interfaces, and (iii) EBSD analyses of the footwall including the sliding surface (Figure 10) with corresponding thin sections (Figure 11).

Figure 4. Temperature evolution during experiments. (a) Temperature increase as a function of slip D, confining pressure for smooth faults (SF) and rough faults (RF) for the two different loading rates tested (f for fast, $1 \, \mu\text{m s}^{-1}$; s for slow, $0.01 \, \mu\text{m s}^{-1}$). Temperature increases raise with the confining pressure, with the coseismic slip and the slip velocity. (b) Temperature signal measured by the thermocouple at 1–2 mm away from the fault during stick-slip motions, at 90 (SF90_s, in green) and 180 MPa (SF180_f, in red) of confining pressure. The temperature increase due to stick-slip motion is fitted (in black) thanks to the inversion model developed by Aubry et al. (2018).

4.1. Macroscopic Aspect of Postmortem Fault Surfaces

Smooth faults deformed from 45 to 90 MPa exhibited either quasi-stable sliding (a unique slip event followed by stable sliding) at a loading rate of $1 \, \mu\text{m s}^{-1}$ (SF45_f and SF90_f) or a stick-slip regime preferentially at a loading rate of $0.01 \, \mu\text{m s}^{-1}$ (SF45_s and SF90_s). Postmortem fault interfaces resulting from these experiments all displayed mirror-like surfaces with highly reflective surfaces and elongated gouge striations parallel to the sliding direction (Figure 5a). At 180 MPa, independently of the loading rates (SF180_f and SF180_s), we observed a stick-slip regime resulting in matte fault surfaces (Figure 5b). These matte fault surfaces exhibited large patches but no visible striations.
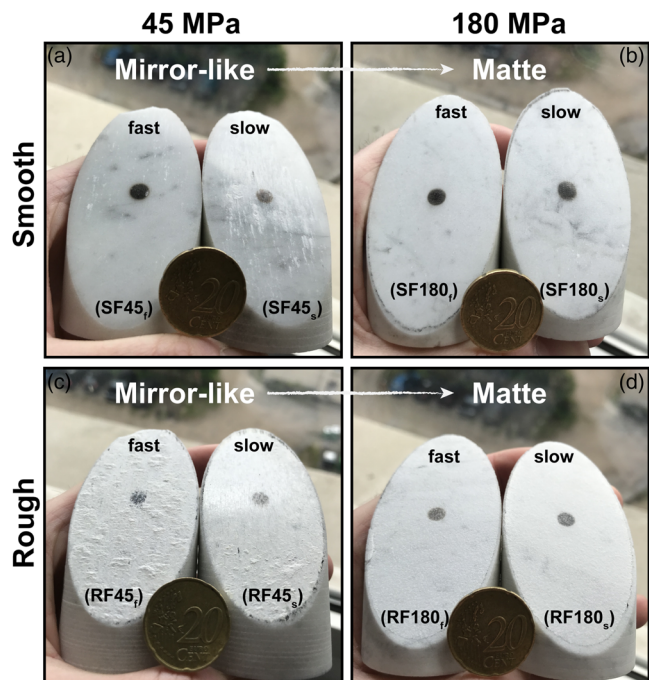
As expected, macroscopic roughness was systematically higher for the experiments conducted on initially rough faults in comparison to the smooth fault interfaces (Figures 5c and 5d). At a fast loading rate ($1 \, \mu\text{m s}^{-1}$), a thick layer of gouge coated the fault interface deformed at 45 MPa (RF45_f), whether shinny striations were discernible after the experiment performed at a slow loading rate (RF45_s; Figure 5c). Rough faults deformed at 180 MPa were also matte (RF180_f and RF180_s; Figure 5d) and the transition from mirror-like surfaces to matte surfaces with increasing confining pressure was also observed.

4.2. Microtopography From Surface Profilometry

Microtopographies measured after experiments are displayed for end-member cases only: (i) initially smooth faults deformed slowly (at $0.01 \, \mu\text{m s}^{-1}$, SF_s; Figures 6b and 6c) which exhibited stick-slip, that is, seismic behavior/unstable slip regime; (ii) initially rough faults, deformed rapidly (at $1 \, \mu\text{m s}^{-1}$, RF_f; Figures 6e and 6f), which exhibited stable sliding (i.e., aseismic behavior/stable slip regime).

The roughness of initially smooth fault interfaces (Figure 6a) systematically increases after the experiments. At 45 MPa (SF45_s), elongated and flattened asperities develop as topographic heights, where gouge particles accumulated (Figure 6b). Conversely, topographic lows appear as wide flattened domains corresponding to the mirror-like surfaces described above (Figure 5). Striations along the sliding direction are visible and crosscut both topographic highs and lows. At 180 MPa (SF180_s), no clear striations are visible and centimeter-sized asperity patches develop, as well as topographic bumps and holes, in directions oblique compared to the slip direction (Figure 6c).

Compared to initially smooth fault surfaces, the roughness of initially rough ones evolves differently (Figure 6d). At 45 MPa (RF45_f), roughness increases as large asperities developed (Figure 6e). These
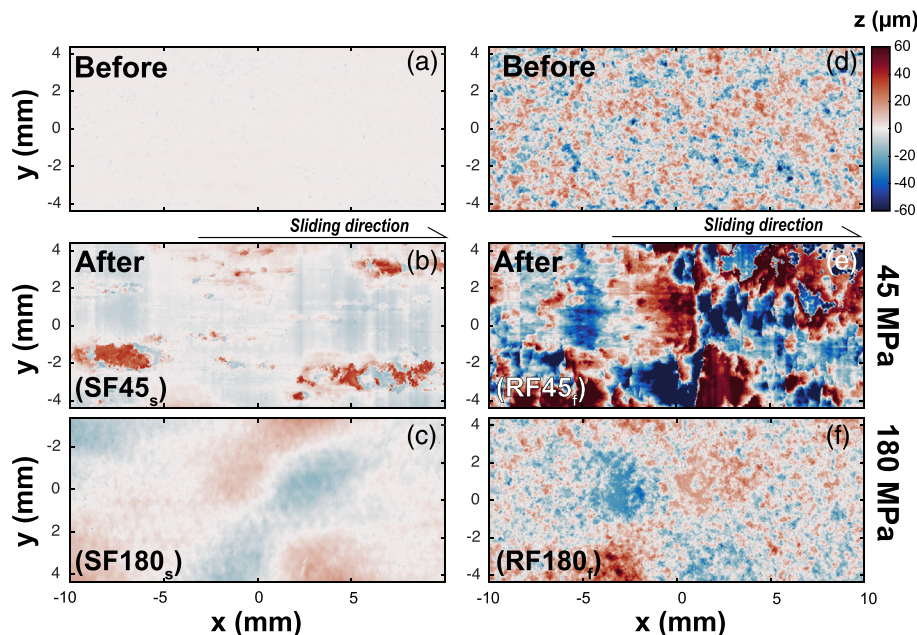
Figure 5. Macroscopic pictures of the footwall of the fault after experiments. A transition from mirror like (SF45$_f$, SF45$_s$, RF45$_f$, and RF45$_s$) to matte surfaces (SF180$_f$, SF180$_s$, RF180$_f$, and RF180$_s$) seems systematic after experiments with increasing confining pressure, whatever the loading rates or the initial roughness of the fault, either smooth (a and b) or rough (c and d). Scale is a quarter of euro coin.

asperities are asymmetric, crenulated, and elongated perpendicular rather than parallel to the sliding direction, forming a stair-case like pavement. In this case, striations crosscut highs and lows. At 180 MPa (RF180$_f$), roughness does not evolve much as the initial roughness pattern can easily be recognized, probably because fault locked due to plastic deformation during the experiment (Figure 6f). Nevertheless, a long wavelength topography emerges, in a similar way than what is observed for initially smooth faults.
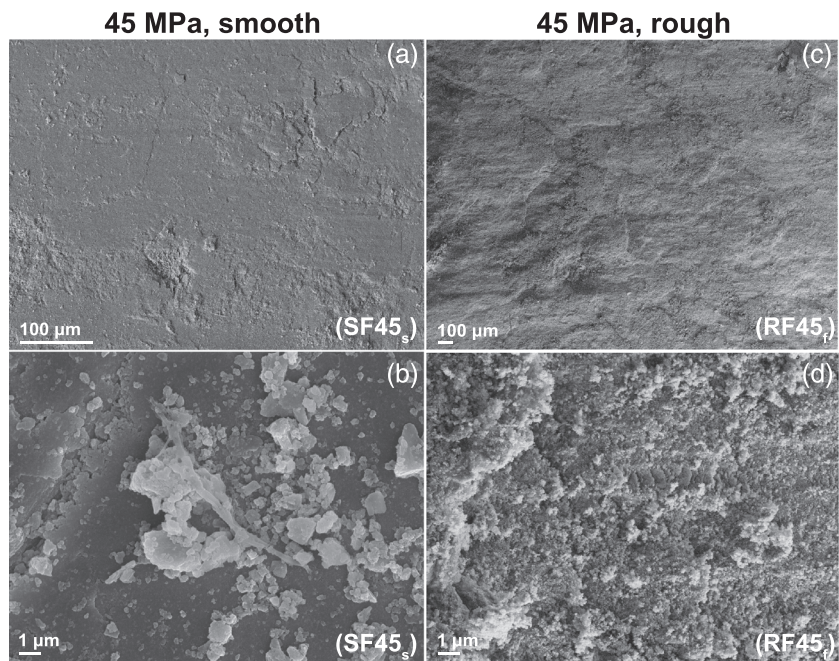
In summary, striations and brittle asperities due to gouge particles accumulation are observed at low pressure. However, asperities are flattened and mirror like only when the fault surface exhibits stable sliding. At high pressure, a large wavelength topography emerges and promotes matte fault surfaces both on smooth and rough faults.

4.3. Scanning and Transmission Electron Microscopy Observations
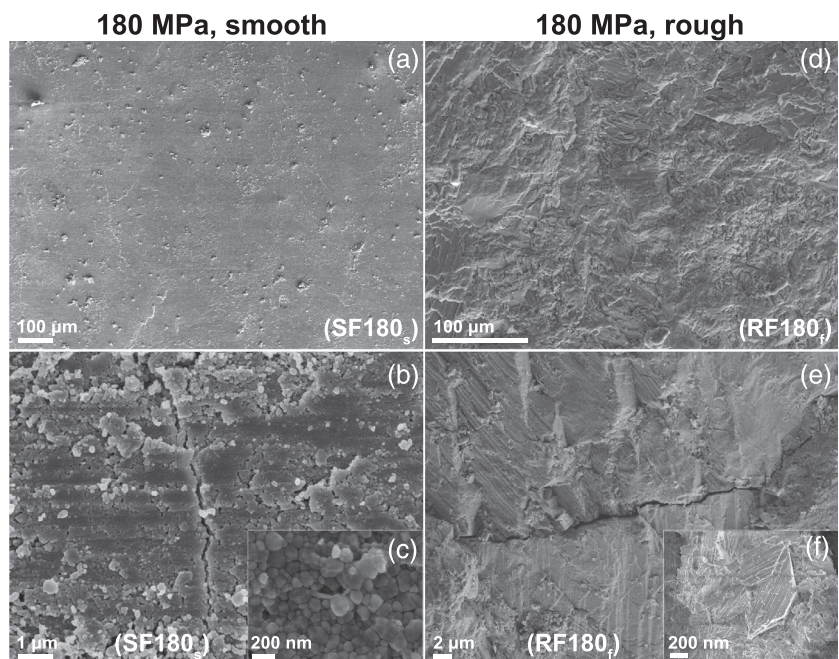
The patterns emerging from the microtopography described above are complemented by microscopic imaging. At low pressure, striations remain visible at the microscale, in both smooth and rough faults (Figure 7). The smooth fault appears polished, with low topography except where gouge particles accumulated to form a scaly fabric, not observed on the entire fault surface (FS45$_s$; Figure 7a). Holes around tens microns length are found in which cataclastic grain were carried by cumulative slips. The fabric is composed of gouge particles typically micrometric or smaller (Figure 7b). In the case of the rough fault, the surface is damaged, with a pervasive scaly fabric (RF45$_f$;
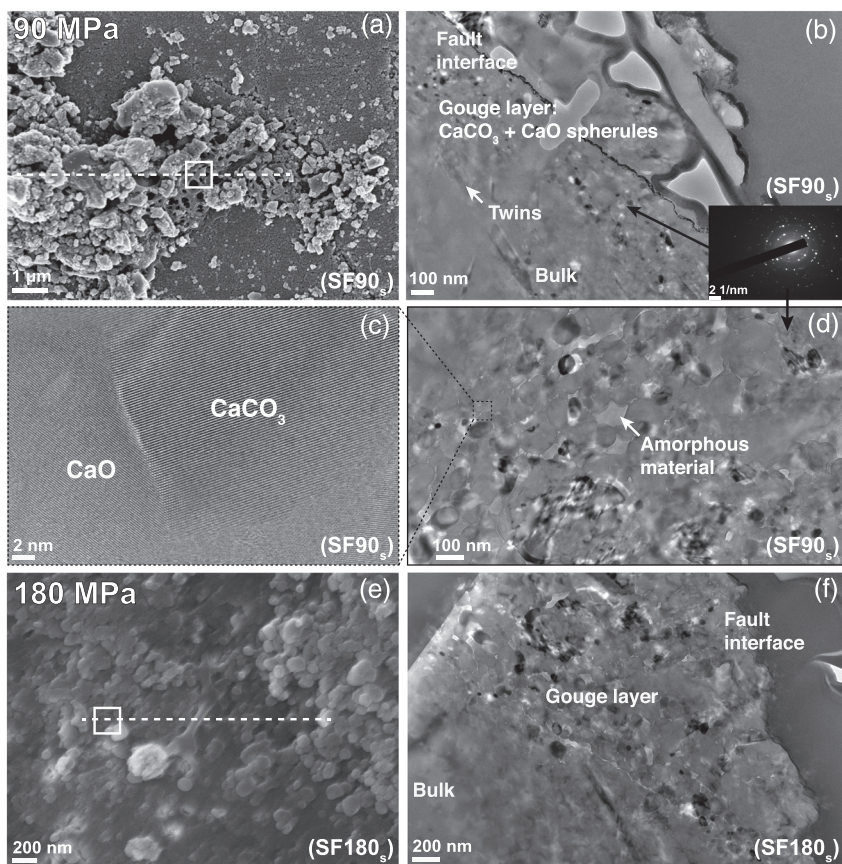

Figure 6. Microtopographies before and after seismic and aseismic experiments. The microtopographies measured by surface profilometry on the footwall samples are presented for smooth-slow loading rates (b and c; SF45$_s$ and SF180$_s$) and rough-fast loading rates (e and f; RF45$_f$ and RF180$_f$) experiments, from 45 to 180 MPa. The initial microtopography of both smooth and rough fault surfaces are displayed in (a) and (d), respectively. With increasing confining pressure, asperities become larger. Sliding direction is toward right. The color bar represents the altitude of the asperities on the fault surface, z (µm).

45 MPa, smooth **45 MPa, rough**

Figure 7. SEM micrographs at low confining pressure. At low confining pressure (45 MPa), striations remain visible the microscale, in both the cases of initially smooth or rough faults (a and c). The initially smooth fault appears polished (SF45$_s$), with little topography except where gouge particles accumulated to form a scaly fabric (a and b). Holes around tens microns length are found in which cataclastic micrometric or smaller grain were found (b). In the case of the rough fault (RF45$_f$), the surface is damaged, with a pervasive scaly fabric (c) with comminuted grains found at smaller scale (d).

180 MPa, smooth **180 MPa, rough**

Figure 8. SEM micrographs at high confining pressure. At high confining pressure (180 MPa), striations are invisible at the millimetric scale (a and d). The initially smooth fault is very polished at large scale (a) and shows a compact network of recrystallized nanoparticles and foam-like porous structure at smaller scale (b and c; SF180$_s$). Rough surfaces exhibit no striations and less gouge particle (d; RF180$_f$) compared to the low-pressure case (Figures 7c and 7d). At the microscale, grains exhibit local "striations" along randomly oriented directions, probably evidence of crystal-plastic deformation (e and f).
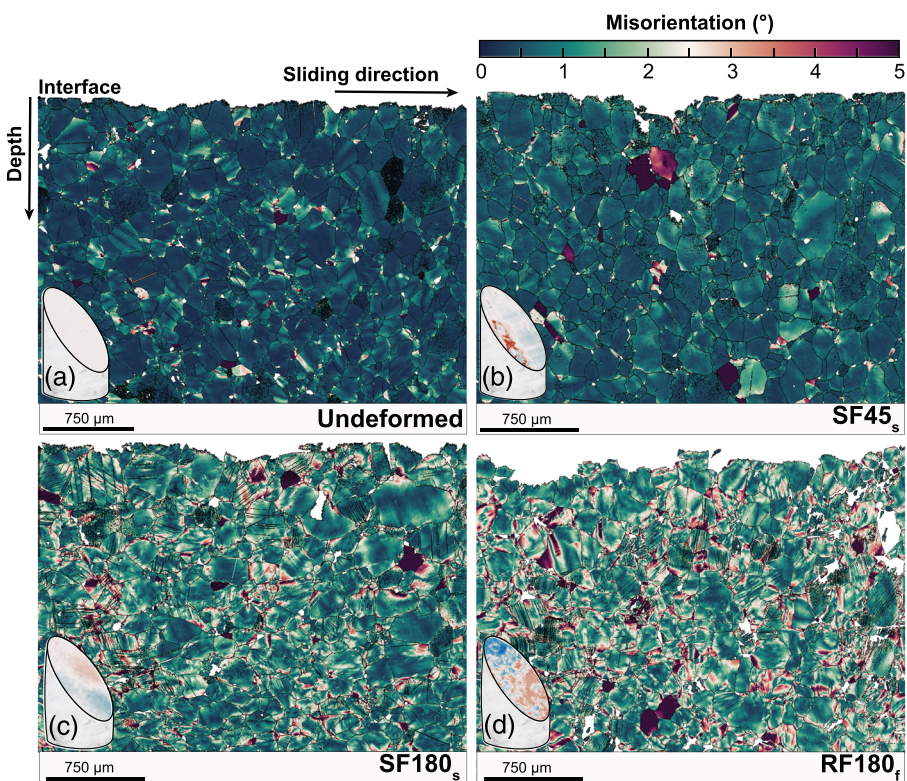
Figure 9. TEM observations on some postmortem fault sections. (a) Micrographs of the fault surface after the 90 MPa and slow loading rate experiment ($SF90_s$), where FIB section has been produced (white dashed line). TEM observations on this section in (b). We found spherules of $CaCO_3$ and CaO on the gouge layer (d) that demonstrate that decarbonation occurred on the fault surface (c). (e) Micrographs of the fault surface after the 180 MPa and slow loading rate experiment ($SF180_s$). With increasing confining pressure, nanograins of the gouge layer become larger (f).

Figure 7c). In this case, gouge particles are smaller than on smooth fault, which indicates a higher degree of grain comminution, and cover the entire surface (Figure 7d).

At high pressure, no striations are observed at the millimetric scale (Figure 8). The smooth fault appears even more polished and with smaller gouge particle clusters ($SF180_s$; Figure 8a) in comparison with the opposite low pressure case (Figures 7a and 7b). At high magnification, the polished surface appears as a fine-grained pavement, composed of compact and euhedral nanoparticles never exceeding 100 nm (Figure 8b). Below this pavement, a foam-like porous structure can be observed (Figure 8c). The presence of amorphous filaments at grain junctions suggests that these grains could result from recrystallization and sintering processes during a fast cooling stage (Figure 8c). This is corroborated by the ubiquitous observation of cracks crosscutting the pavement and, for the most part, oriented perpendicular to the direction of sliding (Figures 8a and 8b). These cracks may be caused by quick cooling and associated thermal cracking. At the millimetric scale, no striations are observed on rough surfaces ($RF180_f$; Figure 8d), most probably because fault slip was limited for these samples. Again, the surface appears scaly but with less gouge particle compared to the low-pressure case. At the microscale, grains exhibit local "striations" along randomly oriented directions, probably evidence of mechanical twinning and crystal-plastic deformation (Figures 8e and 8f).

To further investigate the nanostructure observed at high pressure on initially smooth samples (Figures 8b and 8c), focused ion beam sections were realized at two locations where the foam-like porous structures were observed, respectively, on samples deformed at 90 ($SF90_s$; Figures 9a–9d) and 180 MPa ($SF180_s$;
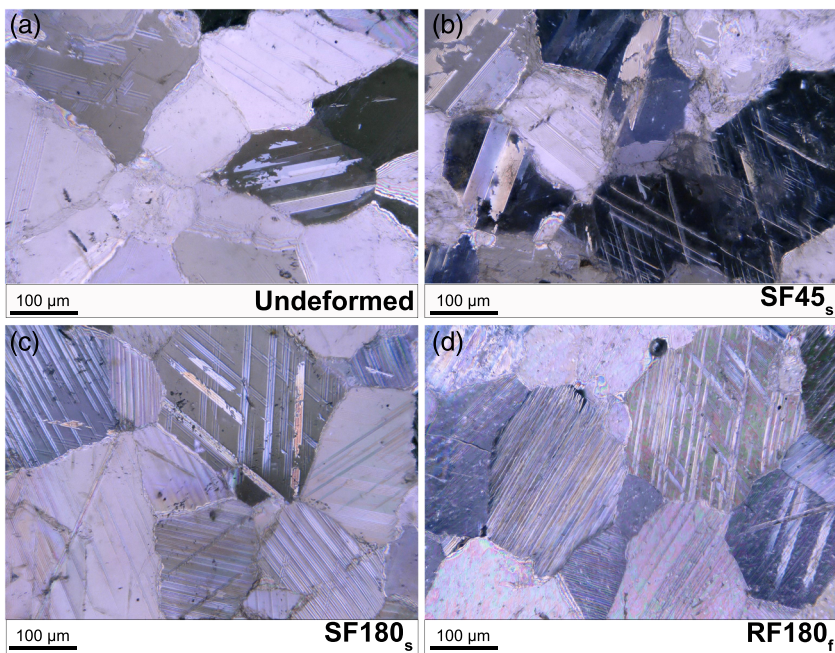
Figure 10. EBSD observations on postmortem fault sections. EBSD map of the misorientation of grain in the undeformed material for (a, b) a smooth fault deformed at 45 at slow loading rates (SF45$_s$), (c) a smooth fault deformed at 180 MPa at slow loading rates (SF180$_s$), and (d) a rough faults deformed at 180 MPa at fast loading rates (RF180$_f$). For each EBSD map, we show the sample deformed after experiment (including microtopography on the fault interface and bulk appearance). Bulk plasticity occurs from 180 MPa when asperities are large in a varnished fault surface (c) and increases with roughness (d).

Figures 9e and 9f). Transmission electron micrographs reveal the presence of twins within a micrometric calcite crystal situated below a nanograin pavement less than a micrometer thick (SF90$_s$; Figure 9b). Some amorphous material is also present within the nanocrystalline layer, as demonstrated by the diffraction pattern of a selected area (Figure 9b). The porous structure of the layer is evidenced at higher magnification (Figure 9c). Finally, high-resolution imagery demonstrates that the layer is composed of a mixture of calcite and lime nanocrystals as well as pores filled by amorphous material (Figures 9c and 9d). Similar conclusions can be drawn for the high pressure sample (SF180$_s$; Figures 9e and 9f), with the notable differences of the nanocrystalline layer being thicker (close to 1 μm), and both the individual crystals and the pores being larger. Combined together, the latter observations demonstrate that frictional heating of the fault surface was intense enough to trigger calcite decarbonation.

4.4. Electron Backscattered Diffraction Mapping

To document plastic bulk deformation, four EBSD maps were collected on sections of the fault-walls of specimen undeformed (Figure 10a), and samples deformed slowly at 45 (SF45s; Figure 10b) and 180 MPa (SF180$_s$ and RF180$_f$; Figures 10c and 10d), respectively. Grain misorientation maps document crystal-plastic deformation and provide information on its spatial distribution relative to the fault surface.

On both types of images, the intensity of intracrystalline plastic strain clearly increases with confining pressure (up to 180 MPa: SF180s) and roughness (RF180$_f$), associated to an increase of twin density and decrease of their thickness (Figure 11). Our observations do not reveal any strain gradient away from the fault (even for a sample which underwent hundreds of slow slips and no evidence of plastic strain on the strain gage record; SF45$_s$), suggesting that plastic strain was accommodated homogeneously within the bulk of the specimen (Figures 10b–10d). Stick-slip events themselves did not produce significant near-field intracrystalline

Figure 11. Thin sections. Thin sections of the undeformed Carrara marble (a, b) of the smooth sample deformed at 45 at slow loading rates (SF45$_s$), (c) of smooth sample deformed at 180 MPa at slow loading rates (SF180$_s$), and (d) of a rough sample deformed at 180 MPa at fast loading rates (RF180$_f$). The thickness of twins seems to decrease with confining pressure, so that their density increase. The presence of intragrains twins is larger for rough conditions.

plastic strain, probably because the high strain rates involved during dynamic rupture propagation were accommodated by microcracking rather than intracrystalline plastic deformation in the bulk of the sample. These observations suggest that plastic strain was accumulated in between stick-slips, that is, during the sticking or interseismic periods. The accommodation of plastic strain is promoted when fault roughness increases and stable slip occurs.
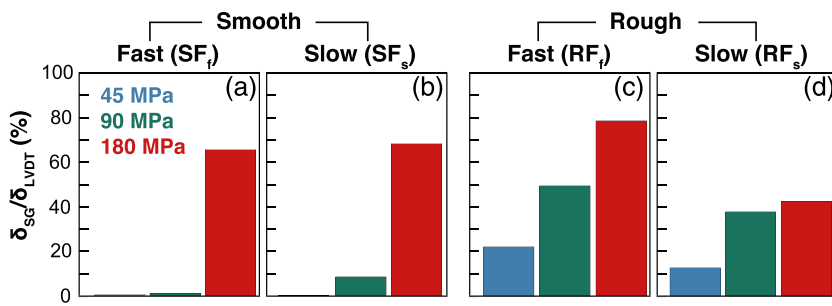
5. Discussion

Our main results highlight (i) that fault stability depends on confining pressure, loading rates and initial fault surface roughness; (ii) a strain partitioning transition between shortening accommodated by fault slip at low pressure and a contribution to strain accommodation by homogeneous plastic deformation and fault slip with increasing pressure and roughness; (iii) the occurrence of stick-slips when crystal-plastic strain was prevalent. Microstructural observations point toward the role played by roughness evolution, frictional heating, and plasticity during frictional sliding.

5.1. Onset of Plasticity and Strain Partitioning

Our experimental results constrain the conditions at which frictional sliding may coexist with plastic deformation. Figure 12 shows a gradual transition from deformation being accommodated exclusively by frictional sliding at low confining pressure (45 MPa, in blue; SF45$_f$ and SF45$_s$), to strain partitioning at 90 (green; SF90$_f$ and SF90$_s$) and 180 MPa (red; SF180$_f$ and SF180$_s$) for initially smooth faults. Note that at 90 MPa (SF90$_s$), the transition occurred during the experiment, with shortening being initially accommodated by fault slip, and followed by strain hardening above the yield stress (Figure 3b). Note that the fraction of bulk sample deformation is limited by the length and the location of the strain gage onto the rock surface.

At 180 MPa, plastic deformation of the bulk accounts for a large part of the total deformation (SF180$_f$ and SF180$_s$; Figures 12a and 12b). According to SEM and EBSD analyses (Figures 8 and 10), bulk plastic deformation is mainly attributed to mechanical twinning, and r-, f- dislocation glide, as observed in previous studies (De Bresser & Spiers, 1993, 1997; Fredrich et al., 1989; Turner et al., 1954). The activation of plastic processes within the bulk is expected in the range of confining pressure tested, and is known to be

Figure 12. Strain partitioning during the experiments. Strain partitioning $\delta_{SG}/\delta_{LVDT}$ as a function of confining pressure for the (a) smooth/fast (SF_f), (b) smooth/slow (SF_s), (c) rough/fast (RF_f), and (d) rough/slow (RF_s) experiments. Colors represent the confining pressure: 45 MPa in blue, 90 MPa in green, and 180 MPa in red. Higher the strain partitioning, larger the accommodation of plastic strain during the experiments. The maximum fraction of plastic strain accommodated within the bulk sample is observed during the experiment performed at fast loading rate with an initially rough fault interface (c; $RF180_f$).

promoted at slow strain rates (Fredrich et al., 1989; Nicolas et al., 2017). A positive correlation is observed between initial roughness and plastic deformation. The largest partitioning between plastic and elastic strains is observed during the experiment performed at fast loading rates with an initially rough fault interface ($SF180_f$; Figure 12c and Table 2). On rough faults, this partitioning is lowered when the loading rate is slow ($SF180_s$; Figure 12d and Table 2).

Faster strain rates enhance plastic strain for initially rough faults (Figure 12c), mainly because higher stresses are attained, while having little effects on initially smooth faults (Figure 12a and Table 2). These new results suggest that the strain partitioning during the seismic cycle at depth is probably more complicated than for within the brittle upper part of the crust. Strain partitioning during semibrittle deformation seems to be not specific to marble (or calcite bearing lithologies) since it was already observed during cataclastic deformation of saw cut samples of porous Berea sandstone by Scott and Nielsen (1991) and on a single fault produced experimentally in a sample of Carrara marble (Meyer et al., 2019).
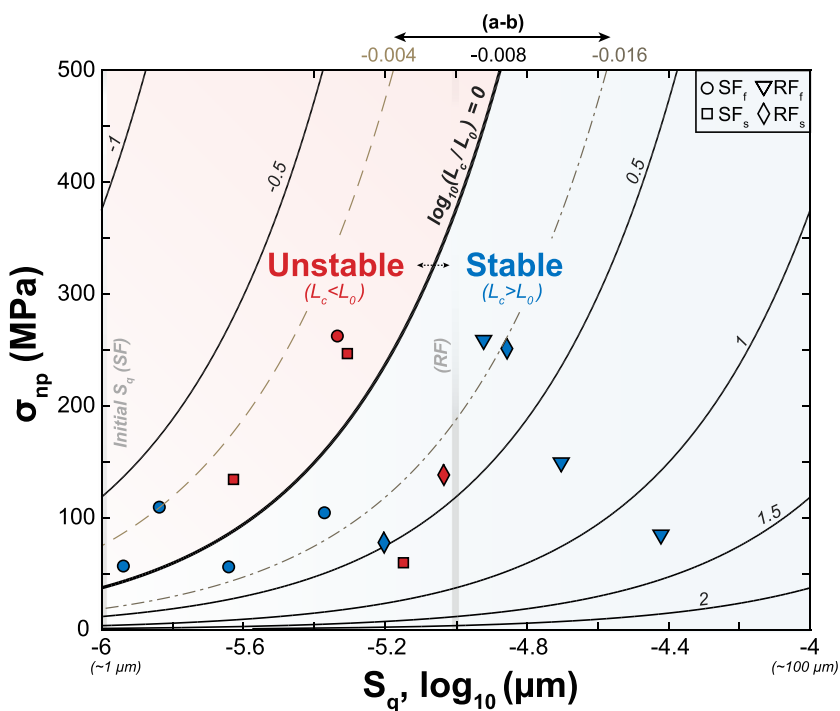
More strain being accommodated within the bulk rather than on the fault also reflects an increase in fault coupling. The strongest laboratory earthquakes were not observed within the brittle regime, where the low confining pressure prevented stress build-up on no coupled faults, but within the semibrittle regime, where confining pressure and plastic strain hardening promoted episodic dynamic fault reactivation at higher shear stresses on coupled faults (Figures 3a and 3c). This may give an insight as to why the largest earthquakes often nucleate at the base of the seismogenic zone (Das & Scholz, 1983; Hobbs & Ord, 1988; Hobbs et al., 1986; Huc et al., 1998; Shimamoto & Logan, 1986).

5.2. Fault Stability, Roughness Evolution, and Plastic Deformation

A widespread way to discuss fault stability comes from rate and state and critical nucleation length concepts (Campillo & Ionescu, 1997; Kanamori & Brodsky, 2004; Latour et al., 2013; Ohnaka & Shen, 1999; Passelègue et al., 2016). Using a simple slip weakening law, the critical nucleation length L_c, above which frictional sliding becomes unstable is given by Kanamori & Brodsky (2004):

$$L_c = \frac{GD_c}{(f_s - f_d)\sigma_n} \tag{1}$$

where G is the shear modulus of the material (Pa), σ_n is the normal stress (Pa), and D_c is the critical slip weakening distance for dynamic stress drop (m) and $(f_s - f_d)$ is the friction drop between static and dynamic friction. Similarly, the transition from aseismic to seismic sliding is generally interpreted in terms of the $(a - b)$ parameter (Ampuero & Rubin, 2008), where a is a parameter interpreting seismic productivity and b, the b value, often used in seismology so that L_c can be also formulated as follows:

Figure 13. Fault stability across the brittle-plastic transition in carbonates. RMS fault roughness S_q as a function of peak normal stress σ_{np} and asperity nucleation size L_c for all experimental data. The transition from aseismic to seismic slip occurs with decreasing S_q, L_C, and increasing σ_{np}. An acceptable boundary is found here for $(a - b) = -0.008$. We also indicate the transition for $(a - b)$ values of -0.004 and -0.016 (dashed and dot dashed lines, respectively). Circles and squares for smooth faults deformed at fast (SF_f) and slow (SF_s) loading rates, respectively. Triangles and rhombus for rough faults deformed at fast (RF_f) and slow (RF_s) loading rates, respectively. Red color for unstable slip regions and experiments; blue color for stable slip regions and experiments (Table 1 and Figure 3). Initial S_q roughness was 1 μm (-6 in log10) and 12.7 μm (-5 in log10) for smooth (SF) and rough faults (RF), respectively.

$$L_c = -\frac{GD_c}{(a - b)\sigma_n} \qquad (2)$$

Therefore, the transition from stable to unstable slip is promoted by increasing pressure (in addition to temperature) and can be interpreted as increasingly negative $(a - b)$. From this concept, the evolution of roughness with slip history is critical in controlling fault stability over the long term. Fault roughness can be quantified, both parallel or perpendicular to slip direction, using the RMS roughness S_q (Bouissou et al., 1998; Bowden & Tabor, 2001; Gadelmawla et al., 2002), which is the root mean square average of the height profiles. This parameter is calculated before and after our experiments:

$$S_q = \sqrt{\frac{1}{A} \int_{x_{min}}^{x_{max}} \int_{y_{min}}^{y_{max}} z^2 \, dx \, dy} \qquad (3)$$

with A, the fault surface area (μm^2) and, z, the height of asperities (μm). The value of the roughness S_q was 1 and 12.7 μm for initially smooth and rough faults, respectively. The value of S_q for initially smooth faults systematically increased after the experiment. On the other hand, for initially rough faults, S_q increased at fast strain rates, that is, when gouge production was prevalent, but decreased at low strain rates (Table 1). The dependence of fault stability regarding the Hurst exponent is under investigation from microtopography data.

Because the critical weakening distance D_c scales with roughness (Marone, 1998; Ohnaka, 2003), we mapped fault slip regime (i.e., stable or instable) as a function of S_q, σ_n, and L_c (Figure 13). For this model, we assumed $G = 24$ GPa, according to $G = \rho V_s^2$, with $\rho = 2{,}710$ kg m^{-3} and $V_s \sim 3$ km s^{-1} as given by Schubnel et al. (2006), and with $(a - b)$ values ranging from -0.004 and -0.016 as measured experimentally in

carbonate gouges (Pluymakers et al., 2016; Verberne et al., 2013). This evidences that our experimental data partition between stable and unstable slip for $(a - b) = -0.008$. We interpret the boundaries between these slip regimes in terms of decreasing asperity nucleation length.

We conclude that unstable slip is favored when $L_c < L_0$ (here, $L_0 = 8$ cm), for low S_q and with increasing σ_n (Passelègue et al., 2019; Scholz, 1998, and references therein; Scott & Nielsen, 1991). Smooth interfaces are prone to be more unstable and efficiently seismically activated (Figure 3a), with the occurrence of events displaying large stress drops (Goebel et al., 2014, 2017; Harbord et al., 2017) because small initial roughness amplitudes promote an increase of stress concentration near the fault interface and asperity yielding (Sagy & Lyakhovsky, 2019). However, no strain gradient away from the fault surface has been observed during our experiments, even at high confining pressure (Figures 10c and 10d).

On the contrary, slip stability and seismic quiescence are promoted at high S_q when $L_c > L_0$ (Harbord et al., 2017; Sagy & Lyakhovsky, 2019). This can be explained by the combined influence of intense gouge production (Marone, 1998) and increasing off-fault plasticity distribution which limited slip on the interface (Figure 6). Note that plastic deformation is more important for rough faults than for smooth ones deformed at high pressure (Figures 3b and 3d and 12). Concurrently, to the increase of contact surface area with normal stress (Badt et al., 2016; Dieterich & Kilgore, 1994; Goebel et al., 2014; Scholz & Engelder, 1976), plastic processes including bulging (Figure 10) and twinning (Figure 11) may favor asperity interlocking (Byerlee, 1967) and rupture arrest (Hok et al., 2010) on rough faults. This process might explain shallow slip deficit on fault zones across the seismogenic zone (Kaneko & Fialko, 2011; Roten et al., 2017).

As explained by Sagy and Lyakhovsky (2019), rough faults are prone to develop aseismic asperities among seismic patches, which stimulate fault reactivation and irregular rupture styles (Bruhat et al., 2016). In this study, we observed that unstable and stable slip can operate together on a smooth (SF; e.g., SF45$_{fl}$) or a rough fault interface (RF; e.g., RF90$_s$). As a number of experimental works before, we observed that fault reactivation is promoted with decreasing sliding velocities (Lockner et al., 1986; Moore et al., 1986; Wong & Zhao, 1990). An important consequence of this observation is that slower deformation in nature should promote fault coupling and unstable frictional sliding.
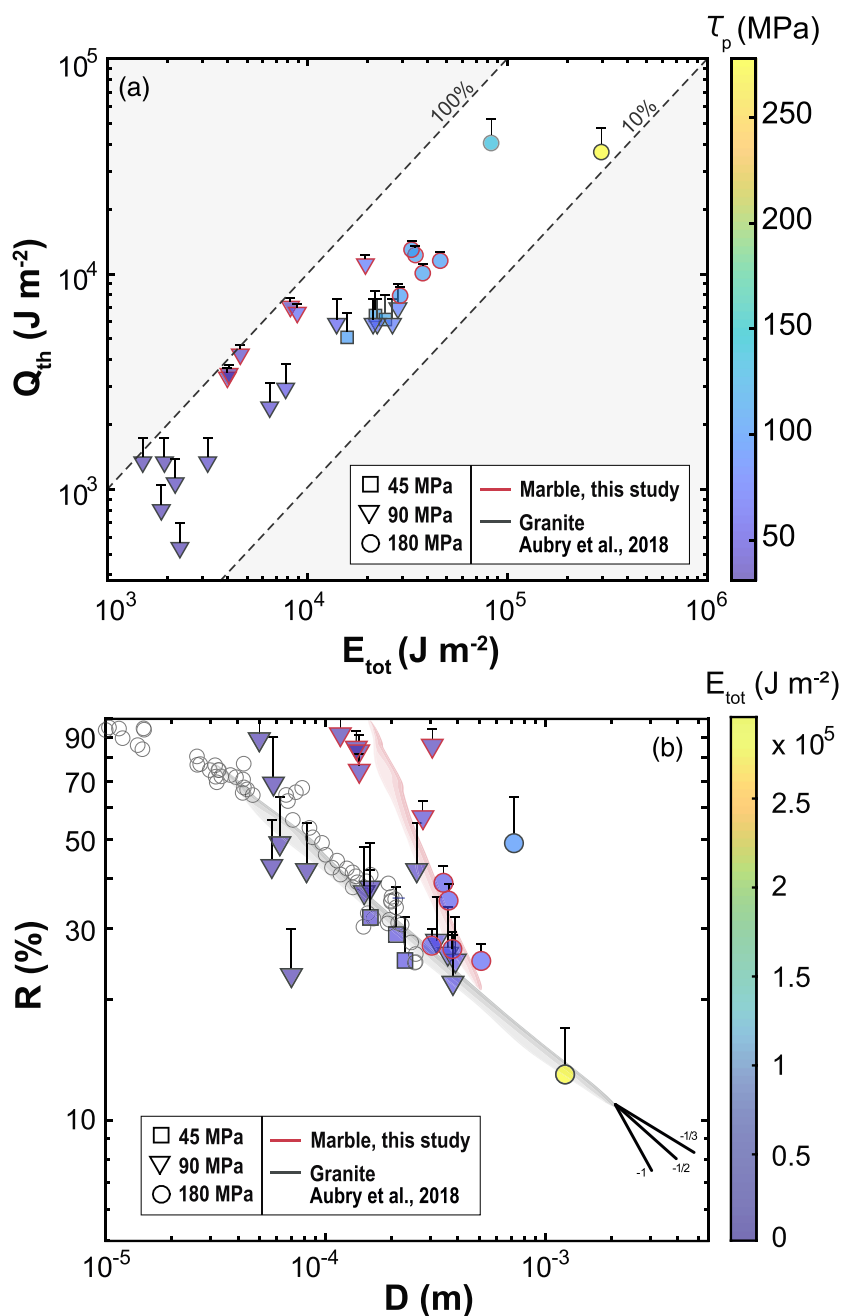
In summary, low roughness and high-normal stress both promote the occurrence of slip instabilities, while highly rough faults tend to remain locked, generally stable and seismically silent. The transition from fault stability to instability is largely controlled by confining pressure and fault roughness, both of which enhancing off-fault stress concentration. With this in mind, we suggest that the predominance of aseismic and stable slip in natural faulting is due to rough, heterogeneous and mature faults, which have large nucleation length, a high capability to produce gouge and off-fault plastic damage.

5.3. Frictional Heating and Dynamics of Faulting Within the Semibrittle Regime

One of the key findings of this study is that stick-slip instabilities can still occur in pressure conditions where plastic deformation of the bulk dominates. We now aim at comparing the energy balance of dynamic faulting within the semibrittle regime, relative to that in a purely elastic-brittle lithology such as Westerly granite (Aubry et al., 2018). In order to quantify the amount of frictional heat produced along the fault interface, we used the method of Aubry et al. (2018) that exploits temperature data recorded by a thermocouple situated a few millimeters away from the fault surface, within the footwall. The frictional heat Q_{th} (J m^{-2}) produced on the interface during stick-slip is defined as follows:

$$Q_{th} = 2\dot{q}_0 t_w \sqrt{\pi \kappa t_w} \tag{4}$$

with $\dot{q}_0$, a constant frictional heat source (in W m^{-3}) for t_w, the typical duration of stick-slip events (about 20 μs; Passelègue et al., 2016) and within the characteristic thermal diffusion length $\sqrt{\pi \kappa t_w}$ (m). A finite difference scheme solving the heat equation in one dimension was used to diffuse heat produced on the interface within the footwall and estimate the temperature rise predicted at the thermocouple location for various values of $\dot{q}_0$. Thermocouple data T_i was interpolated and then inverted using a least squares fit method. The extremely low temperature increases produced by the slow slip events at 45 MPa remained difficult to invert (SF45$_s$). Only a representative subsets of the temperature increases observed during stick-slips at 90 and 180 MPa (Figure 4b) were inverted (Table 3).

Figure 14. Lithology dependence of the energy budget of earthquakes. (a) Frictional heat produced on the fault surface Q_{th} as a function of total mechanical work E_{tot} and peak shear stress τ_p for individual stick-slips in westerly granite (Aubry et al., 2018) and Carrara marble (this study, Table 3). Data from Passelègue et al. (2016) from 10 to 100 MPa of confining pressure in circles in the background. (b) Heating efficiency R as a function of slip D and total mechanical work E_{tot} for the temperature increases due to stick-slip instabilities, considered here. The ratio of available mechanical work converted into frictional heat decreases both with increasing D and available E_{tot}, which suggests a dramatic fault weakening. Higher seismic efficiencies seem to be observed in carbonates than in anhydrous lithologies.

Frictional heat produced during stick-slip is compared to the total mechanical work (Figure 14a), defined as follows:

$$E_{tot} = \frac{(\tau_p + \tau_r)D}{2} \tag{5}$$

with τ_p and τ_r the peak and residual shear stresses (Pa) and, D, the coseismic fault slip (m), that is, the coseismic shortening projected along the fault, corrected for both the rock and the machine's elasticity.

Q_{th} increases with increasing E_{tot} and ranged between 3 and 46 kJ m^{-2} (Table 3). Assuming a thickness of the fault interface twice that of the thermal diffusion length, this translates into fault surface temperatures T_{th} ranging between 100°C and 540°C (Table 3). These temperatures are slightly lower than the range of temperatures expected for decarbonation, between 600°C and 850°C (Han et al., 2010; Rodriguez-Navarro et al., 2009). Furthermore, we note that the thermocouple is an averaged near-fault point measurement. It is thus likely that these temperatures underestimate the temperature reached on local asperities (Aubry et al., 2018).

Interestingly and as previously observed on Westerly granite, the ratio of available mechanical work converted into frictional heat (i.e., heating efficiency R, defined as the ratio Q_{th}/E_{tot}) decreases both with increasing D and available E_{tot}, which suggests dramatic fault weakening after slipping a few tens of microns only (Figure 14b). On fault surfaces that underwent stick-slip motion at high pressure, an ultrathin layer of nanoparticles was found coating the surfaces after the experiment (Figures 8b and 8c). Nanostructural investigations (Figure 9) demonstrated that these layers, less than a micron thick, resulted either from the decarbonation-degassing reaction produced by frictional heating (De Paola et al., 2011; Han et al., 2010; i.e., calcite gives carbon dioxide and lime) and/or the recrystallisation of a carbonated melt. The low viscosity of carbonate melts or the high interstitial pressures expected from decarbonation reactions (Han et al., 2007; Sulem & Famin, 2009) might explain the apparent plateau or saturation observed in the amount of frictional heat produced at high pressure in marble when compared to Westerly granite, which also corresponds to a more dramatic decrease of R (Figure 14b). The higher weakening efficiency observed for carbonates (Figure 14b) is explained by the low melt viscosity of carbonates compared to silicate rocks (Kono et al., 2014). The seismic efficiency (1-R; i.e., the amount of radiated waves vs. mechanical work) of earthquakes might be lithology dependent. In other words, higher seismic efficiency are thus expected in carbonates, dolostones (Passelègue et al., 2019), hydrated rocks such as serpentine (Brantut et al., 2016) than in anhydrous (continental, oceanic, and mantellic) lithologies because of more dramatic weakening.

Finally, we also shed a light on the role played by asperity hardness on fault weakening initiation (Engelder & Scholz, 1976). This discussion comes from the concept of critical weakening velocity V_w developed by Rice (2006), which states that lowering the asperity hardness τ_c leads to an increase of the critical weakening velocity V_w. Combined with the observations of Tabor (1954), who showed that the asperity hardness τ_c of quartz is higher than that of calcite, we emphasize that low asperity hardness promotes higher weakening velocity and potential fault instability on fault rocks.

6. Conclusions

Our experimental work on Carrara marble provides constraints regarding fault stability across the seismogenic zone, at brittle-plastic conditions. A changeover from stable to unstable slip was observed with increasing confining pressure, decreasing roughness, asperity nucleation size, and loading rates. A transition from mirror like to matte surfaces is observed with increasing pressure either on smooth or rough faults for which gouge production was more intense. Further studies could help to extrapolate these observations to natural tectonic strain rates.

Because of plastic strain hardening, the semibrittle regime corresponds to a regime of maximum fault strength, where the most violent laboratory earthquakes were observed. This might give insights as to why large crustal earthquakes may nucleate at the base of the seismogenic zone, on inherited fault interfaces, while country rocks deform in the semibrittle deformation regime. At such high stresses, dynamic fault slip triggers instantaneous and dramatic fault weakening within a few microns of slip, because of the combined effects of decarbonation and shear-induced melting. At similar conditions, fault weakening in carbonates is more dramatic than in silicate rocks, which suggests that the earthquake seismic efficiency has a lithology dependence.

Finally, this study brings some implications on fault coupling maps and seismic moment balance along natural active faults. Indeed, when performing seismic moment balance, geodetic studies often suggest seismic moment deficit, while assuming elastic coupling only, even at depth. Here we show that plastic deformation can coexist with the occurrence of laboratory earthquakes. Within the semibrittle regime (i.e., at depths > 10 km), strain partitioning between fault slip and plastic deformation prevails and is promoted with

increasing initial fault roughness. In these conditions, faults may appear locked and subject to episodic slip, while most of the interseismic moment is nevertheless accommodated by irreversible plastic deformation of the wall rocks.

Conflict of Interest

The authors declare that they have no competing financial interests.

Data Availability Statement

The data that support the findings of this study are available in Mendeley Data at https://doi.org/10.17632/nmbz29y22k.1 website.

References

Amoruso, A., Crescentini, L., Morelli, A., & Scarpa, R. (2002). Slow rupture of an aseismic fault in a seismogenic region of Central Italy. *Geophysical Research Letters*, *29*(24), 2219. https://doi.org/10.1029/2002GL016027

Ampuero, J. P., & Rubin, A. M. (2008). Earthquake nucleation on rate and state faults—Aging and slip laws. *Journal of Geophysical Research*, *113*, B01302. https://doi.org/10.1029/2007JB005082

Aubry, J., Passelègue, F. X., Deldicque, D., Girault, F., Marty, S., Lahfid, A., et al. (2018). Frictional heating processes and energy budget during laboratory earthquakes. *Geophysical Research Letters*, *45*, 12,274–12,282. https://doi.org/10.1029/2018GL079263

Bachmann, F., Hielscher, R., & Schaeben, H. (2010). Texture analysis with MTEX–free and open source software toolbox. In *Solid State Phenomena* (Vol. 160, pp. 63–68). Princeton, NJ: Trans Tech Publications. https://doi.org/10.4028/www.scientific.net/ssp.160.63

Badt, N., Hatzor, Y. H., Toussaint, R., & Sagy, A. (2016). Geometrical evolution of interlocked rough slip surfaces: The role of normal stress. *Earth and Planetary Science Letters*, *443*, 153–161. https://doi.org/10.1016/j.epsl.2016.03.026

Bistacchi, A., Griffith, W. A., Smith, S. A., Di Toro, G., Jones, R., & Nielsen, S. (2011). Fault roughness at seismogenic depths from LIDAR and photogrammetric analysis. *Pure and Applied Geophysics*, *168*(12), 2345–2363. https://doi.org/10.1007/s00024-011-0301-7

Bouissou, S., Petit, J. P., & Barquins, M. (1998). Normal load, slip rate and roughness influence on the PMMA dynamics of sliding 2. Characterisation of the stick-slip phenomenon. *Wear*, *215*(1–2), 137–145. https://doi.org/10.1016/s0043-1648(97)00268-8

Bowden, F. P., & Tabor, D. (2001). *The friction and lubrication of solids* (Vol. 1). New York, NY: Oxford University Press.

Brantut, N., Passelègue, F. X., Deldicque, D., Rouzaud, J. N., & Schubnel, A. (2016). Dynamic weakening and amorphization in serpentinite during laboratory earthquakes. *Geology*, *44*(8), 607–610. https://doi.org/10.1130/g37932.1

Bruhat, L., Fang, Z., & Dunham, E. M. (2016). Rupture complexity and the supershear transition on rough faults. *Journal of Geophysical Research: Solid Earth*, *121*, 210–224. https://doi.org/10.1002/2015JB012512

Byerlee, J. D. (1967). Theory of friction based on brittle fracture. *Journal of Applied Physics*, *38*(7), 2928–2934. https://doi.org/10.1063/1.1710026

Campillo, M., & Ionescu, I. R. (1997). Initiation of antiplane shear instability under slip dependent friction. *Journal of Geophysical Research*, *102*(B9), 20,363–20,371. https://doi.org/10.1029/97JB01508

Chiarabba, C., Amato, A., Anselmi, M., Baccheschi, P., Bianche, I., Cattaneo, M., et al. (2009). The 2009 L'Aquila (Central Italy) M_w 6.3 earthquake: Main shock and aftershocks. *Geophysical Research Letters*, *36*, L18308. https://doi.org/10.1029/2009GL039627

Das, S., & Scholz, C. H. (1983). Why large earthquakes do not nucleate at shallow depths. *Nature*, *305*(5935), 621–623. https://doi.org/10.1038/305621a0

De Bresser, J. H. P., & Spiers, C. J. (1997). Strength characteristics of the r, f, and c slip systems in calcite. *Tectonophysics*, *272*(1), 1–23. https://doi.org/10.1016/S0040-1951(96)00273-9

De Bresser, J. T., & Spiers, C. J. (1993). Slip systems in calcite single crystals deformed at 300–800°C. *Journal of Geophysical Research*, *98*(B4), 6397–6409. https://doi.org/10.1029/92JB02044

De Paola, N., Hirose, T., Mitchell, T., Di Toro, G., Viti, C., & Shimamoto, T. (2011). Fault lubrication and earthquake propagation in thermally unstable rocks. *Geology*, *39*(1), 35–38. https://doi.org/10.1130/G31398.1

Dieterich, J. H., & Kilgore, B. D. (1994). Direct observation of frictional contacts: New insights for state-dependent properties. *Pure and Applied Geophysics*, *143*(1–3), 283–302. https://doi.org/10.1007/BF00874332

Engelder, J. T., & Scholz, C. H. (1976). The role of asperity indentation and ploughing in rock friction—II: Influence of relative hardness and normal load. *In International Journal of Rock Mechanics and Mining Sciences & Geomechanics Abstracts*, *13*(5), 155–163). Pergamon. https://doi.org/10.1016/0148-9062(76)90820-2

Evans, B., Fredrich, J. T., & Wong, T. F. (1990). The brittle-ductile transition in rocks: Recent experimental and theoretical progress. *The Brittle-Ductile Transition in Rocks, Geophysical Monograph Series*, *56*, 1–20. https://doi.org/10.1029/gm056p000

Fang, Z., & Dunham, E. M. (2013). Additional shear resistance from fault roughness and stress levels on geometrically complex faults. *Journal of Geophysical Research: Solid Earth*, *118*, 3642–3654. https://doi.org/10.1002/jgrb.50262

Fondriest, M., Smith, S. A., Candela, T., Nielsen, S. B., Mair, K., & Di Toro, G. (2013). Mirror-like faults and power dissipation during earthquakes. *Geology*, *41*(11), 1175–1178. https://doi.org/10.1130/G34641.1

Fortin, J., Guéguen, Y., & Schubnel, A. (2007). Effects of pore collapse and grain crushing on ultrasonic velocities and Vp/Vs. *Journal of Geophysical Research- olid Earth*, *112*, B08207. https://doi.org/10.1029/2005JB004005

Fredrich, J. T., Evans, B., & Wong, T. F. (1989). Micromechanics of the brittle to plastic transition in Carrara marble. *Journal of Geophysical Research*, *94*(B4), 4129–4145. https://doi.org/10.1029/JB094iB04p04129

Gadelmawla, E. S., Koura, M. M., Maksoud, T. M. A., Elewa, I. M., & Soliman, H. H. (2002). Roughness parameters. *Journal of Materials Processing Technology*, *123*(1), 133–145. https://doi.org/10.1016/s0924-0136(02)00060-2

Galli, P., Galadini, F., & Pantosti, D. (2008). Twenty years of paleoseismology in Italy. *Earth-Science Reviews*, *88*(1-2), 89e117. https://doi.org/10.1016/j.earscirev.2008.01.001

Goebel, T. H., Kwiatek, G., Becker, T. W., Brodsky, E. E., & Dresen, G. (2017). What allows seismic events to grow big?: Insights from b-value and fault roughness analysis in laboratory stick-slip experiments. *Geology*, *45*(9), 815–818. https://doi.org/10.1130/G39147.1

Goebel, T. H. W., Candela, T., Sammis, C. G., Becker, T. W., Dresen, G., & Schorlemmer, D. (2014). Seismic event distributions and off-fault damage during frictional sliding of saw-cut surfaces with pre-defined roughness. *Geophysical Journal International*, *196*(1), 612–625. https://doi.org/10.1093/gji/ggt401

Han, R., Hirose, T., & Shimamoto, T. (2010). Strong velocity weakening and powder lubrication of simulated carbonate faults at seismic slip rates. *Journal of Geophysical Research*, *115*, B03412. https://doi.org/10.1029/2008JB006136

Han, R., Shimamoto, T., Hirose, T., Ree, J. H., & Ando, J. I. (2007). Ultralow friction of carbonate faults caused by thermal decomposition. *Science*, *316*(5826), 878–881. https://doi.org/10.1126/science.1139763

Harbord, C. W., Nielsen, S. B., De Paola, N., & Holdsworth, R. E. (2017). Earthquake nucleation on rough faults. *Geology*, *45*(10), 931–934. https://doi.org/10.1130/G39181.1

Harbord, C. W. A. (2018). *Earthquake nucleation, rupture and slip on rough laboratory faults (Doctoral dissertation)* (pp. 109–161). Durham, UK: Department of Earth Sciences, Durham University. http://etheses.dur.ac.uk/12725/

Hirth, G., & Tullis, J. (1994). The brittle-plastic transition in experimentally deformed quartz aggregates. *Journal of Geophysical Research*, *99*(B6), 11,731–11,747. https://doi.org/10.1029/93JB02873

Hobbs, B. E., & Ord, A. (1988). Plastic instabilities: Implications for the origin of intermediate and deep focus earthquakes. *Journal of Geophysical Research*, *93*(B9), 10,521–10,540. https://doi.org/10.1029/JB093ib09p10521

Hobbs, B. E., Ord, A., & Teyssier, C. (1986). Earthquakes in the ductile regime? *Pure and Applied Geophysics*, *124*(1–2), 309–336. https://doi.org/10.1007/BF00875730

Hok, S., Campillo, M., Cotton, F., Favreau, P., & Ionescu, I. (2010). Off-fault plasticity favors the arrest of dynamic ruptures on strength heterogeneity: Two-dimensional cases. *Geophysical Research Letters*, *37*, L02306. https://doi.org/10.1029/2009GL041888

Huc, M., Hassani, R., & Chéry, J. (1998). Large earthquake nucleation associated with stress exchange between middle and upper crust. *Geophysical Research Letters*, *25*(4), 551–554. https://doi.org/10.1029/98GL00091

Jolivet, R., Lasserre, C., Doin, M. P., Peltzer, G., Avouac, J. P., Sun, J., & Dailu, R. (2013). Spatio-temporal evolution of aseismic slip along the Haiyuan fault, China: Implications for fault frictional properties. *Earth and Planetary Science Letters*, *377-378*, 23–33. https://doi.org/10.1016/j.epsl.2013.07.020

Kanamori, H., & Brodsky, E. E. (2004). The physics of earthquakes. *Reports on Progress in Physics*, *67*(8), 1429–1496. https://doi.org/10.1088/0034-4885/67/8/r03

Kaneko, Y., & Fialko, Y. (2011). Shallow slip deficit due to large strike-slip earthquakes in dynamic rupture simulations with elasto-plastic off-fault response. *Geophysical Journal International*, *186*(3), 1389–1403. https://doi.org/10.1111/j.1365-246X.2011.05117.x

Kohlstedt, D. L., Evans, B., & Mackwell, S. J. (1995). Strength of the lithosphere: Constraints imposed by laboratory experiments. *Journal of Geophysical Research*, *100*(B9), 17,587–17,602. https://doi.org/10.1029/95JB01460

Kono, Y., Kenney-Benson, C., Hummer, D., Ohfuji, H., Park, C., Shen, G., et al. (2014). Ultralow viscosity of carbonate melts at high pressures. *Nature Communications*, *5*(1), 1–8. https://doi.org/10.1038/ncomms6091

Latour, S., Schubnel, A., Nielsen, S., Madariaga, R., & Vinciguerra, S. (2013). Characterization of nucleation during laboratory earthquakes. *Geophysical Research Letters*, *40*, 5064–5069. https://doi.org/10.1002/grl.50974

Lockner, D. A., Kilgore, B. D., Beeler, N. M., & Moore, D. E. (2017). The transition from frictional sliding to shear melting in laboratory stick-slip experiments. *Fault zone dynamic processes: Evolution of fault properties during seismic rupture*, 105–132. https://doi.org/10.1002/9781119156895.ch6

Lockner, D. A., Summers, R., & Byerlee, J. D. (1986). Effects of temperature and sliding rate on frictional strength of granite. In *Friction and Faulting* (pp. 445–469). Basel: Birkhäuser. https://doi.org/10.1007/978-3-0348-6601-9_4

Marone, C. (1998). Laboratory-derived friction laws and their application to seismic faulting. *Annual Review of Earth and Planetary Sciences*, *26*(1), 643–696. https://doi.org/10.1146/annurev.earth.26.1.643

McNulty, B. A. (1995). Pseudotachylyte generated in the semi-brittle and brittle regimes, Bench Canyon shear zone, central Sierra Nevada. *Journal of Structural Geology*, *17*(11), 1507–1521. https://doi.org/10.1016/0191-8141(95)00052-F

Meccheri, M., Molli, G., Conti, P., Blasi, P., & Vaselli, L. (2007). The Carrara Marbles (Alpi Apuane, Italy): A geological and economical updated review. *Z. dt. Ges. Geowiss*, *158*(4), 719–736. https://doi.org/10.1127/1860-1804/2007/0158-0719

Meyer, G. G., Brantut, N., Mitchell, T. M., & Meredith, P. G. (2019). Fault reactivation and strain partitioning across the brittle-ductile transition. *Geology*, *47*(12), 1127–1130. https://doi.org/10.1130/g46516.1

Moore, D. E., Summers, R., & Byerlee, J. D. (1986). The effects of sliding velocity on the frictional and physical properties of heated fault gouge. *Pure and Applied Geophysics*, *124*(1–2), 31–52. https://doi.org/10.1007/BF00875718

Nicolas, A., Fortin, J., Regnet, J. B., Verberne, B. A., Plümper, O., Dimanov, A., et al. (2017). Brittle and semibrittle creep of Tavel limestone deformed at room temperature. *Journal of Geophysical Research: Solid Earth*, *122*, 4436–4459. https://doi.org/10.1002/2016JB013557

Obara, K., & Kato, A. (2016). Connecting slow earthquakes to huge earthquakes. *Science*, *353*(6296), 253–257. https://doi.org/10.1126/science.aaf1512

Ohnaka, M. (2003). A constitutive scaling law and a unified comprehension for frictional slip failure, shear fracture of intact rock, and earthquake rupture. *Journal of Geophysical Research*, *108*(B2), 2080. https://doi.org/10.1029/2000jb000123

Ohnaka, M., & Shen, L. F. (1999). Scaling of the shear rupture process from nucleation to dynamic propagation: Implications of geometric irregularity of the rupturing surfaces. *Journal of Geophysical Research*, *104*(B1), 817–844. https://doi.org/10.1029/1998JB900007

Passelègue, F. X., Aubry, J., Nicolas, A., Fondriest, M., Deldicque, D., Schubnel, A., & di Toro, G. (2019). From fault creep to slow and fast earthquakes in carbonates. *Geollogy*, *47*, 744–748. https://doi.org/10.1130/G45868.1

Passelègue, F. X., Schubnel, A., Nielsen, S., Bhat, H. S., Deldicque, D., & Madariaga, R. (2016). Dynamic rupture processes inferred from laboratory microearthquakes. *Journal of Geophysical Research: Solid Earth*, *121*, 4343–4365. https://doi.org/10.1002/2015JB012694

Paterson, M. S., & Wong, T. F. (2005). *Experimental rock deformation—The brittle field*. Berlin, Heidelberg, Germany: Springer Science & Business Media. https://link.springer.com/book/10.1007/b137431#toc

Peng, Z., & Gomberg, J. (2010). An integrated perspective of the continuum between earthquakes and slow-slip phenomena. *Nature Geoscience*, *3*(9), 599–607. https://doi.org/10.1038/ngeo940

Pluymakers, A. M. H., Niemeijer, A. R., & Spiers, C. J. (2016). Frictional properties of simulated anhydrite-dolomite fault gouge and implications for seismogenic potential. *Journal of Structural Geology*, *84*, 31–46. https://doi.org/10.1016/j.jsg.2015.11.008

Renard, F., Mair, K., & Gundersen, O. (2012). Surface roughness evolution on experimentally simulated faults. *Journal of Structural Geology*, *45*, 101–112. https://doi.org/10.1016/j.jsg.2012.03.009

Rice, J. R. (2006). Heating and weakening of faults during earthquake slip. *Journal of Geophysical Research*, *111*, B05311. https://doi.org/10.1029/2005JB004006

Rodriguez-Navarro, C., Ruiz-Agudo, E., Luque, A., Rodriguez-Navarro, A. B., & Ortega-Huertas, M. (2009). Thermal decomposition of calcite: Mechanisms of formation and textural evolution of CaO nanocrystals. *American Mineralogist*, *94*(4), 578–593. https://doi.org/10.2138/am.2009.3021

Roten, D., Olsen, K. B., & Day, S. M. (2017). Off-fault deformations and shallow slip deficit from dynamic rupture simulations with fault zone plasticity. *Geophysical Research Letters*, *44*, 7733–7742. https://doi.org/10.1002/2017GL074323

Sagy, A., Brodsky, E. E., & Axen, G. J. (2007). Evolution of fault-surface roughness with slip. *Geology*, *35*(3), 283–286. https://doi.org/10.1130/G23235A.1

Sagy, A., & Lyakhovsky, V. (2019). Stress patterns and failure around rough interlocked fault surface. *Journal of Geophysical Research: Solid Earth*, *124*, 7138–7154. https://doi.org/10.1029/2018JB017006

Scarpa, R., Amoruso, A., Crescentini, L., Fischione, C., Formisano, L. A., La Rocca, M., & Tronca, F. (2008). Slow earthquakes and low frequency tremor along the Apennines, Italy. *Annals of Geophysics*.

Scholz, C. H. (1998). Earthquakes and friction laws. *Nature*, *391*(6662), 37–42. https://doi.org/10.1038/34097

Scholz, C. H., & Engelder, J. T. (1976). The role of asperity indentation and ploughing in rock friction—I: Asperity creep and stick-slip. *In International Journal of Rock Mechanics and Mining Sciences & Geomechanics Abstracts*, *13*(8), A86–A154). Pergamon. https://doi.org/10.1016/0148-9062(76)91557-6

Schubnel, A., Fortin, J., Burlini, L., & Gueguen, Y. (2005). Damage and recovery of calcite rocks deformed in the cataclastic regime. *Geological Society, London, Special Publications*, *245*(1), 203–221. https://doi.org/10.1144/GSL.SP.2005.245.01.10

Schubnel, A., Walker, E., Thompson, B. D., Fortin, J., Guéguen, Y., & Young, R. P. (2006). Transient creep, aseismic damage and slow failure in Carrara marble deformed across the brittle-ductile transition. *Geophysical Research Letters*, *33*, L17301. https://doi.org/10.1029/2006GL026619

Scott, T. E., & Nielsen, K. C. (1991). The effects of porosity on the brittle-ductile transition in sandstones. *Journal of Geophysical Research-Solid Earth*, *96*(B1), 405–414. https://doi.org/10.1029/90JB02069

Shimamoto, T., & Logan, J. M. (1986). Velocity-dependent behavior of simulated halite shear zones: an analog for silicates. *See Das et al.*, *37*, 49–63. https://doi.org/10.1029/GM037p0049

Siman-Tov, S., Aharonov, E., Sagy, A., & Emmanuel, S. (2013). Nanograins form carbonate fault mirrors. *Geology*, *41*(6), 703–706. https://doi.org/10.1130/G34087.1

Smith, S. A. F., Nielsen, S., & Di Toro, G. (2015). Strain localization and the onset of dynamic weakening in calcite fault gouge. *Earth and Planetary Science Letters*, *413*, 25–36. https://doi.org/10.1016/j.epsl.2014.12.043

Sulem, J., & Famin, V. (2009). Thermal decomposition of carbonates in fault zones: Slip-weakening and temperature-limiting effects. *Journal of Geophysical Research- Solid Earth*, *114*, B03309. https://doi.org/10.1029/2008jb006004

Tabor, D. (1954). Mohs's hardness scale-a physical interpretation. *Proceedings of the Physical Society. Section B*, *67*(3), 249–257. https://doi.org/10.1088/0370-1301/67/3/310

Tse, S. T., & Rice, J. R. (1986). Crustal earthquake instability in relation to the depth variation of frictional slip properties. *Journal of Geophysical Research- Solid Earth*, *91*(B9), 9452–9472. https://doi.org/10.1029/JB091iB09p09452

Turner, F. J., Griggs, D. T., & Heard, H. (1954). Experimental deformation of calcite crystals. *Geological Society of America Bulletin*, *65*(9), 883–934. https://doi.org/10.1130/0016-7606(1954)65[883:edocc]2.0.co;2

Vajdova, V., Baud, P., & Wong, T. F. (2004). Compaction, dilatancy, and failure in porous carbonate rocks. *Journal of Geophysical Research-Solid Earth*, *109*, B05204. https://doi.org/10.1029/2003jb002508

Vajdova, V., Zhu, W., Chen, T. M. N., & Wong, T. F. (2010). Micromechanics of brittle faulting and cataclastic flow in Tavel limestone. *Journal of Structural Geology*, *32*(8), 1158–1169. https://doi.org/10.1016/j.jsg.2010.07.007

Verberne, B. A., Niemeijer, A. R., De Bresser, J. H., & Spiers, C. J. (2015). Mechanical behavior and microstructure of simulated calcite fault gouge sheared at 20–600°C: Implications for natural faults in limestones. *Journal of Geophysical Research: Solid Earth*, *120*, 8169–8196. https://doi.org/10.1002/2015JB012292

Verberne, B. A., Plümper, O., de Winter, D. M., & Spiers, C. J. (2014). Superplastic nanofibrous slip zones control seismogenic fault friction. *Science*, *346*(6215), 1342–1344. https://doi.org/10.1126/science.1259003

Verberne, B. A., Spiers, C. J., Niemeijer, A. R., De Bresser, J. H. P., De Winter, D. A., & Plümper, O. (2013). Frictional properties and microstructure of calcite-rich fault gouges sheared at sub-seismic sliding velocities. *Pure and Applied Geophysics*, *171*(10), 2617–2640. https://doi.org/10.1007/s00024-013-0760-0

Wong, T. F., & Baud, P. (2012). The brittle-ductile transition in porous rock: A review. *Journal of Structural Geology*, *44*, 25–53. https://doi.org/10.1016/j.jsg.2012.07.010

Wong, T. F., & Zhao, Y. (1990). Effects of load point velocity on frictional instability behavior. *Tectonophysics*, *175*(1–3), 177–195. https://doi.org/10.1016/0040-1951(90)90137-w

Zielke, O., Galis, M., & Mai, P. M. (2017). Fault roughness and strength heterogeneity control earthquake size and stress drop. *Geophysical Research Letters*, *44*, 777–783. https://doi.org/10.1002/2016GL071700